

Pareto-Efficient Quantum Circuit Simulation Using Tensor Contraction Deferral*

Edwin Pednault^{†1}, John A. Gunnels^{†1}, Giacomo Nannicini^{†1}, Lior Horesh¹, Thomas Magerlein², Edgar Solomonik³, Erik W. Draeger⁴, Eric T. Holland⁴, and Robert Wisnieff¹

¹IBM T.J. Watson Research Center, Yorktown Heights, NY

²Tufts University, Medford, MA

³Dept. of Computer Science, University of Illinois at Urbana-Champaign, Champaign, IL

⁴Lawrence Livermore National Laboratory, Livermore, CA

Abstract

With the current rate of progress in quantum computing technologies, systems with more than 50 qubits will soon become reality. Computing ideal quantum state amplitudes for circuits of such and larger sizes is a fundamental step to assess both the correctness, performance, and scaling behavior of quantum algorithms and the fidelities of quantum devices. However, resource requirements for such calculations on classical computers grow exponentially. We show that deferring tensor contractions can extend the boundaries of what can be computed on classical systems. To demonstrate this technique, we present results obtained from a calculation of the complete set of output amplitudes of a universal random circuit with depth 27 in a 2D lattice of 7×7 qubits, and an arbitrarily selected slice of 2^{37} amplitudes of a universal random circuit with depth 23 in a 2D lattice of 8×7 qubits. Combining our methodology with other decomposition approaches found in the literature, we show that we can simulate 7×7 -qubit random circuits to arbitrary depth by leveraging secondary storage. These calculations were thought to be impossible due to resource requirements.

1 Introduction

In the last few years, significant technological progress has enabled quantum computing to evolve from a visionary idea [18] to reality [11, 12]. With existing devices now providing 20–50 qubits with controllable couplings, the potential of quantum devices to perform computational tasks beyond what any classical computer can perform is receiving much attention [25, 38, 6, 1, 17]. Among the many issues faced in advancing quantum computing technology, two are particularly relevant for this paper: (1) the ability to assess the correctness, performance, and scaling behavior of quantum algorithms [21], and (2) the ability to quantify circuit fidelity (e.g., [4, 39, 20, 6, 30]). Fundamental to both is the ability to calculate quantum state amplitudes for all or arbitrarily selected portions of the quantum state—a task whose difficulty grows exponentially in the size of the circuit, in general. This paper presents a new methodology for this task, suitable for calculating entire quantum states, that can handle circuits of much larger size than those that had been presented in the literature prior to an early preprint of this paper [37]. Our

*An earlier version of this paper was called “Breaking the 49-Qubit Barrier in the Simulation of Quantum Circuits”

[†]Corresponding author; pednault@us.ibm.com

[‡]These authors contributed equally.

approach to calculating quantum amplitudes uses a tensor representation [27], combining the flexibility of tensor computations with tensor slicing methods and optimized secondary storage techniques. A first stage of simulation enables final quantum states of limited-depth circuits to be calculated in slices instead of having to materialize entire quantum states in memory. A second stage of simulation enables such limited-depth calculations to be extended to arbitrary depths by leveraging secondary storage in cases where sufficient resources are available.

A key building block of our approach is *tensor contraction deferral*. This technique allows non-adjacent contractions, in addition to the adjacent contractions used in conventional tensor-network-based circuit simulation algorithms (e.g., [32]). Contraction deferral enables the decomposition of circuits into subcircuits that can be simulated independently and then combined to calculate the final quantum amplitudes, reducing resource requirements. It is the central technique of the first preprint of this paper [37]. To demonstrate our methodology, we apply it to *universal random circuits* constructed according to the rules described in [6]. These circuits can be embedded in a 2D lattice of qubits with nearest-neighbor couplings, and are restricted to gates belonging to the set $\{H, CZ, X^{1/2}, Y^{1/2}, T\}$. The depth of such a circuit is the number of layers that the circuit can be partitioned into, in such a way that at any given layer at most one gate acts on any given qubit. As in [6], the depth count does not include the first layer of Hadamard gates, nor the final layer of Hadamard gates in the revised benchmarks of [31, 43].

We simulate two quantum circuits constructed according to the rules described in [6]: one with depth 27 for a 7×7 grid of qubits, the other with depth 23 for an 8×7 grid of qubits. Simulations were performed in September 2017 at Lawrence Livermore National Laboratory on the Vulcan supercomputer, an IBM Blue Gene/Q system. The primary data structures employed in the depth-27 simulation require just over 4.5 Terabytes of main memory to store results, and just over 3.0 Terabytes for the depth-23 simulation. In contrast, state-of-the-art techniques in existence at the time [24] would have required 8 Petabytes and 1 Exabyte, respectively. Recent work [7, 15, 29, 13, 31, 43, 14, 44, 23, 45] has improved upon our results and simulated larger circuits. A majority of these papers use tensor contraction methods of some form, which we analyze from the point of view of contraction deferral in order to provide a unifying perspective. Although we do not simulate circuits constructed according to the revised rules described in [31, 43], we use our approach to provide a quantitative analysis of the impact of the rule changes on the difficulty of simulation. We also present extensions of our simulation technique in order to combine it with the decomposition approach discussed in [24]. The goal of these extensions is the simulation of quantum circuits with greater depth than discussed above. We show, for example, that 7×7 circuits can in principle be fully simulated with all amplitudes calculated to arbitrary depth in reasonable time (e.g., less than a day for a depth-83 circuit) by leveraging secondary storage. We do not test these extensions computationally, but we describe the foundations of the methodology and estimate the computational resources that these experiments would require. The simulation of 7×7 circuits to arbitrary depth was previously thought to be out of reach [6, 29, 13].

2 Methods

The majority of this paper is devoted to a high-level description of the simulation methodology introduced in this paper; further details are provided in the Supplementary Information.

2.1 Simulation methodology: preliminaries

The input of a simulation algorithm is a description of a quantum circuit, and a specification of a set of amplitudes (i.e., coefficients of the quantum state obtained at the end of the circuit) that have to be computed; we are mainly interested in the case in which all amplitudes have to be computed, but we will address the case of single-amplitude calculations as well. To test and debug the implementation

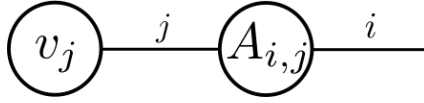


Figure 1: Example of a tensor network for the expression $\sum_j A_{i,j} v_j$.

of a quantum algorithm, having access to the entire quantum state via exact simulation is preferable to computing amplitudes for specific (e.g., measured) outcomes, because this allows the identification of properties of the outcome distribution that cannot be inferred from a small number of samples.

Our analysis considers a hierarchy of storage devices, which has two levels in its simplest form: primary storage, i.e., RAM, and secondary storage, i.e., disk. Descending the hierarchy increases available space but decreases access speed: the performance of a simulation strategy should take into account space occupancy and number of accesses at all levels of the hierarchy. This distinction is crucial from a practical point of view. For example, the full quantum state of a 49-qubit system requires 2^{49} complex numbers (8 PB in double precision); this eliminates the possibility of keeping the entire state in primary storage, but does not rule this out for secondary storage. Thus, disk usage must be allowed in order to have enough space to store the simulation output for circuits of this (or larger) size. To do so, computations must be reorganized to minimize disk access. The main numerical experiments discussed in this paper employ only main memory to store intermediate results, but the Supplementary Information describes how this approach can be extended so that disk can be used to simulate 7×7 -qubit and potentially larger circuits to arbitrary depth. It is well known that a single amplitude can be computed using linear space and exponential time (i.e., number of floating point operations) using the Feynman path approach, see e.g., [1]. However, the time requirement of such an approach grows to intractable levels very quickly with increasing circuit size. We desire exact simulation algorithms with manageable time requirements (i.e., hours – not days), which from a practical standpoint implies a small number of floating point operations per amplitude per gate. This requirement leads us to consider how to best exploit memory hierarchies.

In very broad terms, our approach consists of partitioning a quantum circuit into subcircuits that can be simulated independently and then recombined to obtain the desired result. Of course, a quantum circuit cannot in general be split into subcircuits to be simulated independently due to entanglement. However, when the action of the circuit is represented in a purely algebraic manner, e.g., using a graphical model known as a tensor network [27, 32], it can be verified that arbitrary splitting into subcircuits can be performed, although it may require additional memory and/or computation to account for entanglement between subcircuits. As a consequence, not all decompositions of a circuit into subcircuits are memory-efficient and/or computationally efficient.

A description of our simulation algorithm requires some preliminary discussion regarding tensor networks. A *tensor* is a multilinear map (i.e., a multidimensional generalization of a matrix), equipped with a set of indices to address its elements; each index varies within a specified range, which we always assume to be the set $\{0, 1\}$ in this paper — corresponding to the basis elements $|0\rangle, |1\rangle$ for the vector space \mathbb{C}^2 in which the state of a single qubit lives. The number of indices of a tensor is called its *rank*. It follows that a rank- k tensor with ranges $\{0, 1\}$ requires $O(2^k)$ storage. A *tensor network* is a graph $G = (V, E)$ in which each node is associated with a tensor and each edge with an index of the adjacent tensor(s). Edges between nodes represent shared indices that must be summed over. For example, one possible way to represent a matrix-vector multiplication in a tensor network is shown in Fig. 1. The edge j between the tensors $A_{i,j}$ and v_j represents the operation $\sum_j A_{i,j} v_j$. A summation over shared indices is called a *contraction*.

The tensor network associated with a quantum circuit contains a tensor for each gate, a tensor for the initial state of each qubit, and (optionally) a tensor for the output state under consideration on those qubit lines for which the outcome $\langle 0|$ or $\langle 1|$ has been specified. Edges follow the qubit lines. In this paper we consider only single and two-qubit gates, without loss of generality since any quantum gate can be approximated to arbitrary precision using only single and two-qubit gates. A single-qubit gate is represented as a rank-2 tensor (one edge entering, one edge leaving the associated node), corresponding to a 2×2 matrix, and a two-qubit gate is represented as a rank-4 tensor (two edges entering, two edges leaving), corresponding to a 4×4 matrix.

State-of-the-art algorithms for quantum circuit simulation are for the most part based on the tensor network representation of circuits as described above, which we will refer to as *circuit graphs*. A seminal work in the area is [32], describing a simulation algorithm that runs in time exponential in the treewidth of the line graph of a circuit graph (the treewidth of the line graph is within a constant factor of the treewidth of the corresponding circuit graph). Numerical experiments with this methodology are presented in [19]. After the first preprint of this paper was posted on arXiv, a series of recent works [7, 15, 29, 13, 31, 43, 14, 44, 23, 45] have tackled the problem, increasing the size or depth of circuits that can be simulated; we will discuss the techniques used in these papers after describing our approach. The best known upper bounds on the computational complexity of simulating quantum circuits of the class studied in this paper are given in [1].

2.2 Simulation methodology: main building blocks

We propose an approach that builds on the foundations of tensor networks, with some generalizations to allow for more flexibility in the calculations, especially when we are interested in computing the entire state vector rather than single amplitudes. Three ideas are crucial for our approach: (1) using hyperedges to exploit diagonal (or, more in general, separable) gates, (2) allowing contractions between non-adjacent nodes of the tensor network, and (3) tensor slicing. The first two ideas are not explicitly discussed in the literature on tensor networks for quantum circuit simulation, to the best of our knowledge; slicing is used in [24]. We describe these ideas below.

Formally, we call a gate *diagonal* if the associated tensor $A_{i_1, \dots, i_m, j_1, \dots, j_m}$ is nonzero only if $i_k = j_k$ for $k = 1, \dots, m$; this is a generalization of the concept of diagonal matrices, translated to tensors. For example, the 2×2 identity matrix is a diagonal gate. We call a gate *separable* if it can be obtained from a diagonal gate with a permutation, i.e., there exist functions f_1, \dots, f_m such that $A_{f_1(j_1, \dots, j_m), \dots, f_m(j_1, \dots, j_m), j_1, \dots, j_m}$ is diagonal. For a diagonal gate, because all elements outside the diagonal are zero, it is convenient to assign the same index label to input and output edges, writing the tensor as $A_{i_1, \dots, i_m, i_1, \dots, i_m}$. This representation is not only natural, but also more economical in that it reduces the total number of index labels. We remark that in the case of a sequence of diagonal gates, the same index label could be associated with multiple edges spanning across multiple nodes of the tensor network. Thus, rather than representing the tensor network as a graph, we use a directed *hypergraph*, in which each hyperedge consists of an ordered sequence of nodes and is associated with a single index label. A hyperedge consisting of just two nodes is equivalent to an edge in the original tensor network. We give examples of this representation in Figs. 2 and 3. Conceptually, separable gates can be treated in the same way as diagonal gates: the only difference is that computationally we must keep track of the permutation whenever the tensor corresponding to the gate is applied. Thus, we could represent the example of Fig. 3 with the same hypergraph as in Fig. 2, but any tensor operation with a separable, non-diagonal gate requires accounting for the permutation so that output indices are appropriately computed. For the circuits used in the large-scale simulations discussed in this paper, all separable two-qubit gates are also diagonal or diagonalizable with a straightforward basis change, hence we discuss diagonal gates only in the following.

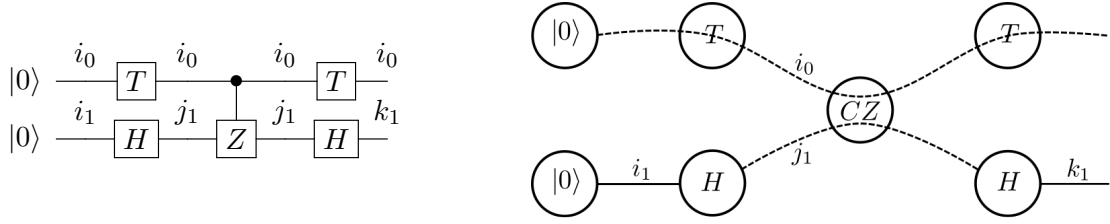


Figure 2: Example of the proposed tensor network representation of a quantum circuit (left), using a hypergraph (right). The T and CZ gates are diagonal. Dashed edges are hyperedges, solid edges are “regular” edges, i.e., hyperedges of cardinality two.

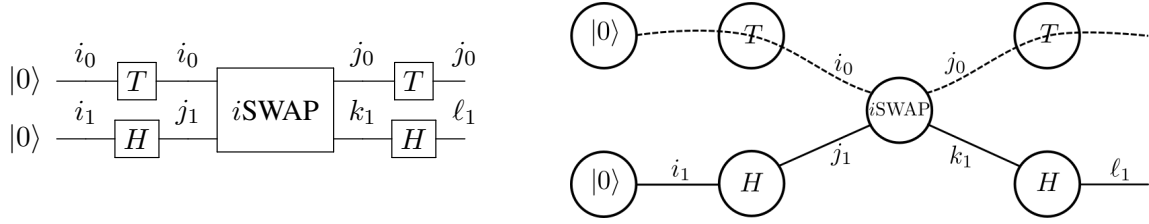


Figure 3: Example of the proposed tensor network representation of a quantum circuit (left), using a hypergraph (right). The T gates are diagonal, i SWAP is not (although it is separable). Dashed edges are hyperedges, solid edges are “regular” edges; i.e., hyperedges of cardinality two.

This representation of the tensor network as a hypergraph allows us to compute tensor ranks that more accurately correspond to the real memory occupancy in a computer implementation of the simulation algorithm. Indeed, a rank- k diagonal tensor requires only $O(2^{k/2})$ memory, as compared to $O(2^k)$ for non-diagonal tensors; consequently, it is incident to $k/2$ hyperedges. This type of consideration plays a crucial role when determining how to partition a tensor network into manageable subgraphs (corresponding to subcircuits). The savings become clear in constructing the line graph of the proposed hypergraph: the line graph of a diagonal two-qubit gate (e.g., controlled-Z gate) is a 4-clique in the traditional tensor network representation, but is only a 2-clique in the proposed representation. This contributes to reducing the treewidth; more details are given in the Supplementary Information.

The second idea that is crucial for our method is the contraction of non-adjacent nodes in the hypergraph. As mentioned earlier, existing simulation methodologies based on tensor networks rely on determining a sequence of contractions between adjacent vertices that leads to the contraction of the entire graph to a single node [32, 7]. In our setting, this is not a viable approach. Since we are interested in determining the whole state vector for an n -qubit system, rather than a single amplitude, a straightforward application of a sequential tensor contraction method would lead to tensors of size proportional to 2^n simply due to the number of open ranks; i.e., the edges at the end of the circuit that are not connected to an output state $\langle 0|$ or $\langle 1|$. We instead allow the non-adjacent contraction of arbitrary sets of nodes in the hypergraph. Such a contraction performs the usual summation over shared indices (i.e., edges interior to the set being contracted), and applies an outer product to the non-shared indices. This approach provides additional flexibility in the order in which contractions are performed to further reduce memory requirements.

In broad terms, we partition the tensor network into sub-hypergraphs corresponding to subcircuits, each of which includes fewer qubits than the initial circuit. Because our end goal is to compute all (or most) amplitudes, we perform computations within each subcircuit following the “Schrödinger approach” [1]; that is, starting from the initial state (i.e., the generalized contraction of the tensor $|0\rangle$ for the qubits under consideration, corresponding to an outer product), we apply layers of quantum gates

one at a time. If there are any two-qubit gates connecting (“bridging”) two different subcircuits, we can choose to defer one of the two corresponding (adjacent) contractions until a subsequent stage of the computation. This *contraction deferral* is accomplished via a non-adjacent contraction that leaves open ranks in the corresponding tensors, increasing memory consumption, but avoids merging potentially large subcircuits. Eventually the subcircuits have to be merged (contracted) to compute the final quantum state, or to initialize the state of a subsequent tensor in the circuit.

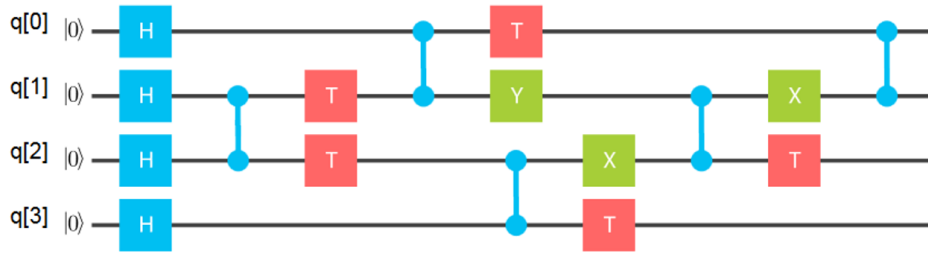
The simulation strategy described in [36] provided the original motivation for contraction deferral. This strategy involves “pulling a grid circuit apart into individual ‘bristle brushes,’ one for each qubit, then computing the corresponding tensors, and finally combining the tensors for each qubit to calculate the quantum amplitudes for the overall circuit.” An example is shown in Fig. 4¹. If we take the individual qubit lines to correspond to subcircuits, tensors corresponding to entangling gates must be assigned to exactly one of the subcircuits that they bridge. The choice can be made arbitrarily but it can have computational implications. The construction of per-qubit tensors involves non-adjacent contractions of gate tensors to effectively jump over entangling gates that were assigned to other qubit lines, as indicated with dashed lines in Fig. 4. An example of contraction deferral is given in Figs. 5(a) and 6(a). As illustrated, contraction deferral introduces *entanglement indices* to account for yet-to-be-resolved entanglements among subcircuits.

To the best of our knowledge, the first paper on quantum circuit simulation to use a form of contraction deferral is [1]. In fact, the use of contraction deferral is not limited to the strategy discussed above, and is independent of the order of contraction. We demonstrate this fact in the Supplementary Information by showing how circuit decompositions based on [1], together with a bidirectional contraction order, can in principle be used to calculate single amplitudes of 7×7 , depth 46 circuits using 141 TB of memory in a matter of a few hours on Vulcan-class supercomputers. In that case, the contractions proceed from both the initial and final states inward, toward the middle, and contraction deferral is employed in both directions.

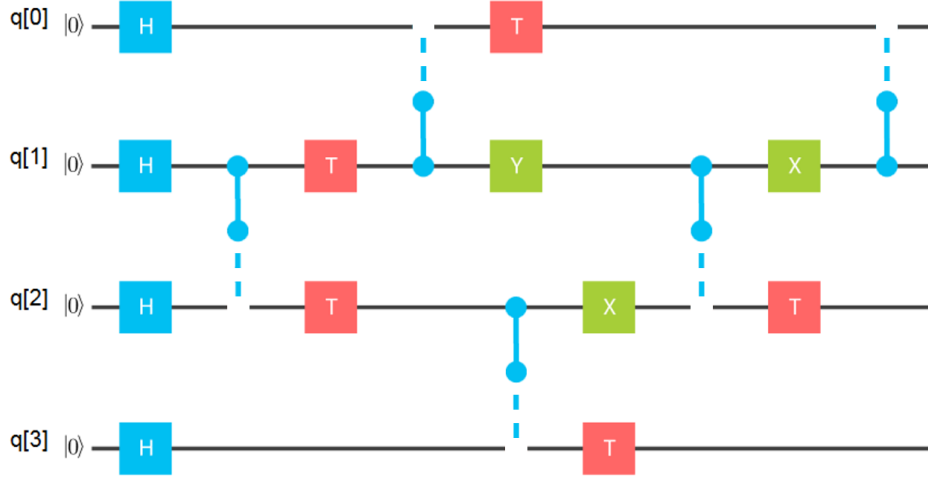
The third and final building block of our methodology is tensor slicing. The idea is to select certain hyperedges in the hypergraph, say s of them, loop over the 2^s possible combinations of values for these hyperedges, and perform the remaining computations with the value for these hyperedges fixed. This yields 2^s “sliced” tensors. If the choice is made appropriately, the resource consumption of each sliced tensors is a factor 2^s smaller than the whole circuit. Since there are 2^s sliced tensors, it may seem that this does not yield any savings; however, our approach tries to reorder the tensor computations so that only a few selected slices (rather than the full tensor) need reside in primary storage, thus decreasing resource consumption and better exploiting parallelism. We also utilize slicing to make the use of secondary storage viable by minimizing data transfer between primary and secondary storage. Our scheme extends the simulation strategy in [24]: we choose a set of qubits to slice, looping over every possible combination of their values, and a superset of those qubits to efficiently index secondary storage. Depending on whether or not slicing is applied to a hyperedge whose contraction is deferred, we distinguish between *sliced contraction deferral* and regular (i.e., non-sliced) contraction deferral. Figs. 5(b) and 6(b) provide examples of sliced contraction deferral applied to the tensor networks of Figs. 2 and 3. It should be noted that, while sliced contraction deferral reduces the memory footprints needed to calculate subcircuit tensors, it does not reduce the memory requirements for storing and summing the contraction results, nor does it reduce the computational requirements. While we did not use sliced contraction deferral in our simulations, it is a key component of the recent literature (see next section), hence it is important to highlight it. The mathematical details of our approach are provided in the Supplementary Information, where we formalize our methodology and use the circuit shown in Fig. 4 as a running example to illustrate further ideas.

We now provide several examples of slicing to illustrate the trade-offs involved that affect overall

¹The name “bristle brushes” comes from [36]; see also Fig. 3 of [43] and [44].



(a) A 4x1 random quantum circuit



(b) “Bristle-brush” subcircuits formed by pulling the circuit apart along qubit lines

Figure 4: Example from [36] extended to illustrate the complete partitioning of a quantum circuit into “bristle-brush” subcircuits divided along qubit lines. The dashed lines correspond to *entanglement indices* that are shared between tensors constructed for each qubit line. Figures 14 and 16 in the Supplementary Information describe alternative ways of partitioning this circuit that yield different computation/memory trade-offs during simulation.

performance. Consider the $8 \times 8 \times (1 + 8 + 1)$ circuit in the GRSC repository [31, 5], which is a 8×8 -qubit, depth 8 circuit with an additional layer of Hadamard gates at the start of the circuit and another at the end of the circuit. We can simulate this circuit as follows. We first construct subcircuits (tensors) for the individual qubit lines, using the “bristle-brush” strategy. Per [36], we then contract these tensors into four 4×4 subcircuits as indicated in Fig. 7(a). Each resulting subcircuit tensor has 16 output indices and 8 entanglement indices, yielding double-precision memory footprints of $2^{16+1 \cdot 8+4} = 256$ MB each. We finally calculate the individual output amplitudes by setting the values of the output indices according to a desired amplitude, thereby slicing the four intermediate tensors; this yields four tensor slices of size $2^{1 \cdot 8+4} = 4$ KB each, which are contracted to yield the desired amplitude.

In general, it is desirable to perform tensor slicing operations as early in a simulation as possible, because doing so can reduce memory requirements without necessarily increasing the number of floating-point operations that are performed per amplitude calculated. In the above example, we can slice the output index of the initial tensors corresponding to the qubit lines *before* contracting them into the 4×4 subcircuits. This early slicing approach reduces the maximum memory footprints of the 4×4 subcircuits from 256 MB to 4 KB each.



Figure 5: (a) *Left*. An example of contraction deferral: the contraction operation on index j_1 in the tensor network of Fig. 2 is deferred. Standard adjacent contractions are performed to construct the upper tensor $U_{i_0, j_1} = T_{i_0} C Z_{i_0 j_1, i_0 j_1} T_{i_0} \delta_{i_0}$ (we denote each tensor by the name of the corresponding gate, and denote the single-index Kronecker delta by δ_k). A non-adjacent contraction is performed on the Hadamard gates to construct the lower tensor $L_{k_1, j_1} = H_{k_1, j_1} \sum_{i_1 \in \{0,1\}} H_{j_1, i_1} \delta_{i_1}$. Contraction deferral allows the top and bottom tensors, U_{i_0, j_1} and L_{k_1, j_1} , to be computed independently. The final state is obtained by contracting j_1 . We refer to indices whose contractions are deferred as *entanglement indices*, in recognition of the fact that they account for the entanglements that exist among subcircuits while allowing those subcircuits to be simulated independently. In this example, j_1 is an entanglement index. (b) *Right*. An example of sliced contraction deferral: a deferred contraction is combined with the slicing of entanglement index j_1 . For each $j_1 \in \{0,1\}$, the top and bottom tensors, U_{i_0, j_1} and L_{k_1, j_1} , are computed independently and their values are multiplied together. The resulting products are then summed over the values of j_1 . The contraction operation on j_1 is thus accomplished iteratively. Because j_1 is fixed at each iteration, the tensors U_{i_0, j_1} and L_{k_1, j_1} are sliced on j_1 and the amount of memory needed to store the slices is cut in half.

If we apply the same strategy to the $8 \times 8 \times (1+40+1)$ circuits in the GRSC repository (i.e., 64-qubit, depth 40 circuits with initial and final layers of Hadamard gates), the corresponding four subcircuits require $2^{5 \cdot 8+4} = 16$ TB of memory each, assuming early slicing of the output indices as described above. Contracting these four tensors in pairs (i.e., A with B, followed by C with D, followed by AB with CD) requires an additional 16 TB of temporary memory to hold intermediate calculations, resulting in a total memory footprint of 80 TB for this final stage of calculation. In the case of $7 \times 7 \times (1+40+1)$ circuits partitioned as shown in Fig. 7(b), subcircuit D requires 16 TB while each other subcircuit requires at most 0.5 TB. The temporary space needed to perform the final contractions is 0.5 TB, yielding a total memory footprint of 18 TB for the final stage of calculation.

Although such memory footprints fit comfortably within the resources available on current classical computers, the computational demands entailed by the above simulation strategy are quite high. For $7 \times 7 \times (1+40+1)$ circuits, the first two of the final contractions (i.e., tensors A with B and C with D) require 2^{50} and 2^{55} complex multiplications and additions per amplitude, while the final contraction requires 2^{35} . Taken together, this translates to approximately 2^{58} floating-point operations per amplitude. For $8 \times 8 \times (1+40+1)$ circuits, the three final contractions together require approximately 2^{61} complex multiplications and additions per amplitude, or 2^{64} floating-point operations per amplitude. In the case of the 7×7 depth 27 circuit whose simulation we present later, the above strategy requires approximately 2^{40} floating-point operations per amplitude for the final three contractions, using a memory footprint of only 4.9 GB. However, to compute all 2^{49} amplitudes, these contractions would require at least 4,168 years to complete at the 5 PFlops/sec peak performance of the Vulcan supercomputer employed in our simulations, which is clearly infeasible. To achieve our objective of computing all amplitudes, we therefore optimize the circuit partitioning at the expense of increased memory requirements to make more efficient use of contraction deferral and significantly speed up the calculations, reducing the number of floating-point operations per amplitude to $2,916 \approx 2^{11.5}$, a factor of $\approx 2^{28.5}$ times less computation.



Figure 6: (a) *Left*. An example of contraction deferral: the contraction operation on indices j_1, k_1 in the tensor network of Fig. 3 is deferred. Standard adjacent contractions are performed to construct the upper tensor $U_{j_0, j_1 k_1} = T_{j_0, j_0} \sum_{i_0 \in \{0,1\}} i\text{SWAP}_{j_0 k_1, i_0 j_1} T_{i_0, i_0} \delta_{i_0}$. A non-adjacent contraction is performed on the Hadamard gates to construct the lower tensor $L_{\ell_1, j_1 k_1} = H_{\ell_1, k_1} \sum_{i_1 \in \{0,1\}} H_{j_1, i_1} \delta_{i_1}$. Contraction deferral allows the top and bottom tensors, $U_{j_0, j_1 k_1}$ and $L_{\ell_1, j_1 k_1}$, to be computed independently. The final state is obtained by contracting j_1 and k_1 . In this example, j_1 and k_1 are entanglement indices. (b) *Right*. An example of sliced contraction deferral: a deferred contraction is combined with the slicing of entanglement indices j_1, k_1 . For each $j_1, k_1 \in \{0, 1\}$, the top and bottom tensors, $U_{j_0, j_1 k_1}$ and $L_{\ell_1, j_1 k_1}$, are computed independently and their values are multiplied together. The resulting products are then summed over the values of j_1 and k_1 . Because j_1 and k_1 are fixed at each iteration, the tensors $U_{j_0, j_1 k_1}$ and $L_{\ell_1, j_1 k_1}$ are sliced on j_1, k_1 and the amount of memory needed to store the slices is cut by a factor of four.

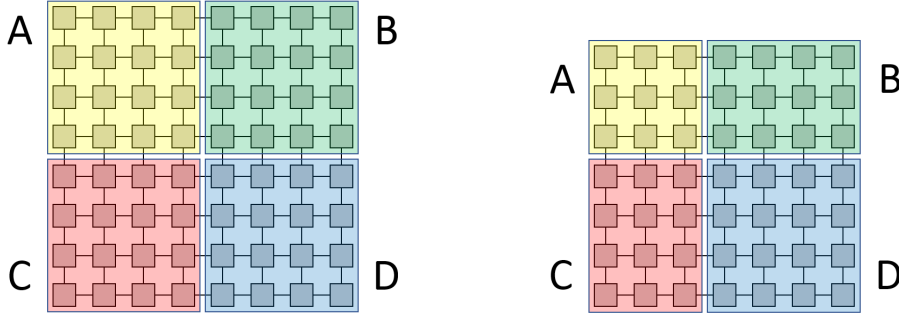


Figure 7: (a) *Left*. Partitioning of an 8×8 -qubit circuit into four 4×4 -qubit subcircuits when the circuit is viewed along the qubit lines (i.e., down the axes of the “bristle brushes”). (b) *Right*. Corresponding partitioning for a 7×7 -qubit circuit.

The optimization methodology is discussed in a subsequent section.

2.3 Tensor contraction deferral in the literature

Before turning our attention to the question of optimization, we review the recent literature on quantum circuit simulation methods based on tensor networks, to provide a unifying perspective showcasing the importance of contraction deferral and slicing, also when combined together.

Sliced contraction deferral, or an equivalent methodology, is used in [15, 29, 13, 31, 43, 44, 45] to reduce both memory requirements and interprocessor communication. In a majority of these methods, the reductions achieved enable all intermediate tensor slice computations to fit within the memories of individual processing nodes for the circuits simulated, thereby eliminating the need for interprocessor communication except to perform final summations of the resulting tensor products. This approach has the benefit of maximizing the degree of parallelism that can be achieved while simultaneously eliminating communication overhead, which in some applications can be orders of magnitude greater than that of

the computations. However, small memory footprints (and accompanying low communication requirements) can come at the cost of very high computational requirements, as the “bristle-brush” strategy demonstrates; hence, such approaches do not guarantee superior performance.

In [43, 44], sliced contraction deferral is applied in combination with non-sliced contraction deferral. Circuits are first contracted along qubit lines to produce grids of per-qubit tensors; these per-qubit tensors correspond to the example in Fig. 4, and their construction requires contraction deferral. Grids of per-qubit tensors are then “cut” [43] into subcircuits using “systematic tensor slicing” [44] (i.e., sliced contraction deferral), thereby enabling the subcircuits to be contracted independently before the final merge; this subcircuit decomposition corresponds to the approach outlined in [36]. Because these subcircuits share a large number of entanglement indices for deep circuits, the use of sliced contraction deferral leads to a significant reduction in both memory requirements and interprocessor communication.

The approach presented in [13, 45] uses a “variable fixing” operation that is a contraction slicing method. It is applied both across qubit lines to entangling gates, as discussed in this paper, and to along-qubit-line indices as in the depth-wise slicing strategy of [1]. [13, 45] uses an optimization algorithm to determine which contractions should be deferred through slicing. Contractions that are not sliced are performed using an extension of the approach in [32] generalized to efficiently handle diagonal gates. Because [32] and [13, 45] only consider adjacent contractions, they explore different circuit decompositions from what is proposed in this paper. The inclusion of depth-wise slicing first introduced in [1] is also a unique characteristic of this approach, relative to other tensor-network approaches.

Taken together, the approaches presented in [43, 44] and in [13, 45] have been used to simulate some of the largest benchmark circuits considered to date.

Interestingly, sliced contraction deferral across qubit lines is not directly considered in [1]. Instead, [1] introduces a gate decomposition approach that is also employed — with some variations — in [15, 29, 31]. As mentioned in [31], gate decomposition can be understood in terms of the Schmidt decomposition of a matrix. In the context of 4×4 matrices, for any matrix $M \in \mathbb{C}^{4 \times 4}$, there exist matrices $U_k, V_k \in \mathbb{C}^{2 \times 2}$ and nonnegative reals $s_k \in \mathbb{R}_+$, $k = 1, \dots, 4$, such that $M = \sum_{k=1}^4 s_k U_k \otimes V_k$. This equation can be obtained from the singular value decomposition of (a permutation of) M . Notice that the Schmidt rank could be strictly less than four; i.e., some s_k could be zero. Thus, a two-qubit gates can be decomposed into a sum of tensor products of single-qubit (not necessarily unitary) matrices. The decomposition can be substituted directly in the tensor equations that define a circuit, enabling subcircuits to be simulated independently without increasing memory footprints, just as in sliced contraction deferral. We remark that gate decomposition in its most general form is different from sliced contraction deferral. However, the gate decompositions considered in [15, 29, 31] are a special case that can be seen as equivalent. Indeed, all three methods employ the CZ -gate decomposition:

$$CZ = |0\rangle\langle 0| \otimes I + |1\rangle\langle 1| \otimes Z. \quad (1)$$

This is also a form of sliced contraction deferral. By rewriting the gate decomposition in tensor form $CZ_{jk,jk} = \delta_{j,0} + \delta_{j,1}Z_{k,k}$, where $\delta_{m,n}$ is the two-index Kronecker delta, it becomes evident that the index j is effectively sliced by the Kronecker deltas and its contraction is performed at the end of the computation, as indicated in [29]. The gate decomposition is instead used in its most general form within the Projected Entangled Pair States (PEPS) approach presented in [23]; this approach computes a PEPS for the final quantum state by directly applying the single-qubit matrices obtained from the singular value decomposition of the two-qubit gates. A tensor network computation is still necessary to perform a projective measurement on the final PEPS, but it does not have a precise correspondence to sliced contraction deferral.

To the best of our knowledge, there is no single implementation that tries to combine all of the circuit-decomposition methods discussed above, and it seems clear that an efficient optimization algorithm to

determine the best strategy, within the large space of all possibilities, could have a large impact on practical performance.

2.4 Optimizing the circuit simulation strategy

In general, due to the large number of possible circuit decompositions, several considerations need to be taken into account to determine an appropriate simulation execution strategy. These considerations will be discussed next.

For a given input quantum circuit, there is an exponentially large number of possible ways of partitioning circuits and sequencing the computations. Additionally, for every non-diagonal entangling gate whose contraction could potentially be deferred, we have the choice of keeping it as is, or transforming it through circuit rewriting to either: diagonalize the gate so as to reduce the number of entanglement indices that would be introduced (e.g., such as transforming a CX gate into two Hadamard gates and one CZ gate); or apply gate decomposition in cases where the minimum number of terms in the decomposition (the Schmidt rank of the gate) is less than the size of the contraction summation induced by the corresponding entanglement indices (i.e., 4 in the case of non-diagonal two-qubit gates). These options generate a space of possible computation schemes for any given circuit. Given a circuit and a computation scheme, we can compute the memory and floating-point operations required simply by analyzing subcircuits. In principle, we would like to run a multi-objective optimization over the space of possible computation schemes to generate the Pareto frontier that defines the optimal trade-off between memory usage and floating-point operations. It is desirable to have an automated process to determine an optimal computation scheme, and it is clear that a brute force exploration strategy of all combinations is not viable for circuits above a modest size.

To obtain the numerical results presented in this paper, we employ two heuristic search strategies: one that implements some hand-crafted circuit partitioning criteria based on our intuitions, and one that explores the choices described above in a largely depth-first manner. The hand-crafted strategies adopt the following principles:

- Diagonalize CX gates if contraction deferral is being applied, or if all subsequent gates applied to the control qubit are diagonal or diagonalizable.
- Try to keep each circuit partitioned into a small number of (e.g., less than five) subcircuits, with a small number of gates crossing the boundaries.

The Supplementary Information illustrates how the 49-qubit, depth 27 random circuit and the 56-qubit, depth 23 random circuit used in our numerical study are partitioned into subcircuits using the hand-crafted approach described above.

We also use a largely depth-first heuristic search to explore the trade-off between memory usage and floating-point operations for various circuits. The method works as follows. It is given a circuit and an upper bound to the memory consumption allowed for the simulation of that circuit. Iteratively, the heuristic selects a two-qubit gate that bridges a pair of subcircuits that have not yet been merged. It then creates two decision branches: one in which the two subcircuits are merged by performing a contraction, the other one in which the contraction is deferred. A decision branch can be pruned if it results in exceeding the memory consumption allowed. The search space is explored using A^* [26], where the heuristic function to assign node potentials is given by a lower bound on the total number of floating point operations resulting from the remaining decisions. Since the lower bound employed is quite weak, we maintain multiple A^* search queues representing different ranges of search depths. We process the search queues in a probabilistic round-robin fashion that favors greater search depths, resulting in a largely depth-first search guided by the A^* heuristic. A lower bound on the number of remaining floating-point operations can be readily obtained by calculating the costs of applying any remaining gates

assuming that the existing tensors will not increase in size; i.e., by treating any remaining entangling gates that bridge existing subcircuits as if they do not bridge them and instead lie solely within one of the subcircuits being bridged.

We note that the above, largely depth-first, search algorithm is the same as the one referenced in our early preprint [37], and as such it considers only non-sliced contraction deferral across qubit lines. The results presented here using the above algorithm thus serve as baselines that illustrate the extent to which non-sliced contraction deferral across qubit lines contributes to resource-efficient quantum circuit simulation. The memory footprints reported take into account all primary tensor data structures that would need to be allocated and de-allocated during the course of simulations, but they exclude the communication buffers typically present in distributed implementations. The reported floating-point operations per gate per amplitude are determined by simply counting the float-point operations (FLOPs) that would need to be performed for the corresponding circuit partitionings. These averages consider the case in which all amplitudes are to be calculated. Communication costs are not included in the assessment.

Fig. 8 illustrates the trade-off between memory and computation identified by this analysis for the 49-qubit, depth 27 and 56-qubit, depth 23 circuits presented in the Supplementary Information that were used in our simulation study. For both circuits, the trade-offs reach the lowest FLOPs (per gate per amplitude) with relatively low memory requirements (i.e., 3.78 FLOPs at 8.5 TB for the 49-qubit circuit and 2.69 FLOPs at 249 GB for the 56-qubit circuit), and we could not improve upon these values even when larger tensors were allowed. Remarkably, these curves remain relatively flat as the allowed memory footprint is decreased, reaching only 3.95 FLOPs per gate per amplitude with a 162 GB memory allowance for the 49-qubit circuit and 3.42 FLOPs with a 4.6 GB memory allowance for the 56-qubit circuit. By comparison, a complex multiply requires six floating-point operations: four multiplications and two additions. For both circuits, computational costs rise sharply when memory thresholds are decreased below these levels, producing “bends” in the curves. Because smaller memory footprints imply less interprocessor communication and greater opportunity for parallelism, some of the simulation strategies identified in in Fig. 8 would likely lead to significantly lower execution times for the simulations as compared to the strategies that we actually ran. Note also that, since the A^* search strategy employed was given a time limit, it is possible that this curve is suboptimal and circuit partitioning schemes that strictly dominate those in Fig. 8 could potentially be found. In addition, the search complexity for our A^* implementation increases as the memory threshold is decreased, owing to the fact that the lower bound on remaining computation incorporated into our A^* heuristic becomes weaker for smaller memory thresholds. As a result, the time limit prevents additional circuit partitionings to be identified below the memory levels indicated in Fig. 8. We note, however, that the memory-efficient “bristle-brush” strategy lies within the search space considered by the A^* algorithm, so in principle these memory thresholds could be lowered much further given sufficient search time.

Complementing the A^* approach outlined above, we develop an integer programming model to search for an optimal circuit partitioning. The model is based on the hypergraph representation discussed above, and it can be solved with existing integer programming software. In the Supplementary Information, we describe the full model and report on our computational experience using the IBM ILOG CPLEX optimization package to solve the instances of the integer programming model corresponding to the two circuits discussed above. Although we cannot solve these problem instances to global optimality within a few hours, the software finds partitioning schemes very similar to the one that we used, and we are able to report bounds on the quality of these partitionings. The A^* approach and the integer programming model can be used to automatically determine an efficient partitioning for a given circuit.

The methodologies presented above concern the determination of a circuit partitioning. When secondary storage is used, it is crucial to organize data on disk in an effective way, which in general differs

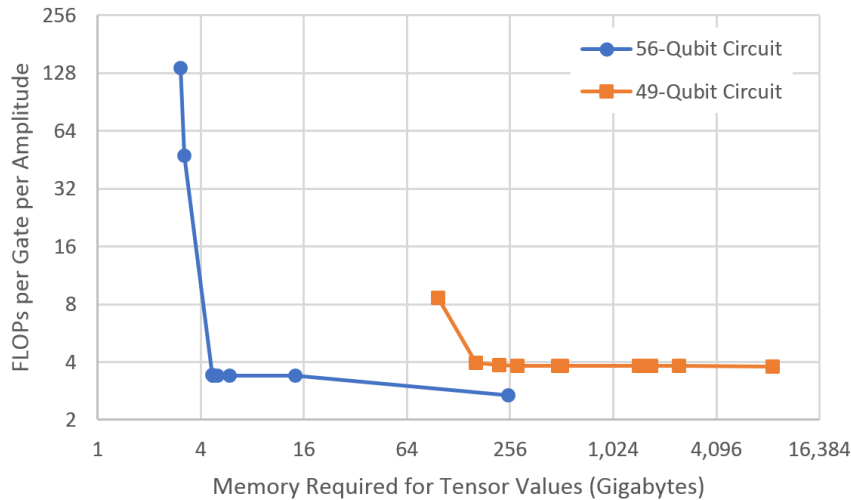


Figure 8: Trade-off between floating point operations and memory usage when employing only non-sliced contraction deferral across qubit lines.

from how it is organized in primary storage. This is because data organization on secondary storage must remain static throughout a simulation. The Supplementary Information presents a greedy optimization method for simultaneously choosing circuit partitionings and data layouts on secondary storage to reduce overall cost.

2.5 Software and hardware platform

We implement the in-memory quantum circuit simulation approach described above using the Cyclops Tensor Framework (CTF) [41], a distributed-memory C++ library for tensor summations and contractions. The library provides a domain-specific language for tensor operations using an Einstein-summation syntax. CTF tensors are distributed over all processors with tensor summations and contractions performed in a data-parallel manner using MPI [22], OpenMP [16], and BLAS [28].

The massively-parallel tensor-contraction calculations enabled by CTF have heretofore been driven by applications in computational chemistry and physics [2, 35] that involve contractions of tensors of rank 4–8; the quantum circuit models employed in our calculation use tensors of much higher rank. In performing these contractions using CTF, the main challenge is the need for higher-dimensional virtual topologies (i.e., the decomposition of tensors among more dimensions) than CTF typically performs. CTF operates by mapping tensor dimensions onto dimensions of a processor grid, often redistributing tensors to new mappings at contraction time. As each index in our tensor corresponds to a qubit in the underlying circuit, mappings to high-dimensional virtual processor grids are necessary. To achieve these, we increase the space of virtual topologies CTF considers, improve the mapping logic in CTF, and enable dynamic creation and destruction of MPI communicators (defined for each processor grid dimension).

We use the built-in profiling capabilities of CTF and the performance-counter libraries made available on the hardware platform we use in our experiments to determine the bottlenecks CTF encounters during circuit simulation contractions [33]. For reasons of brevity, we do not describe all optimizations in this paper. Local copy, summation, and multiplication primitives are automatically replaced by appropriate optimized variants, chosen with knowledge of the parameters in use during the circuit simulations. These low-level changes substantially improve the performance with respect to the original

implementation.

Our experiments are executed on Vulcan, a 24,576-node IBM Blue Gene/Q supercomputer [42]; a brief description of this architecture follows. A Blue Gene/Q node consists of 18 A2 PowerPC 64 bit cores, 16 of which are application-accessible. Each A2 core runs at 1.6 GHz, has a 16 KB private level 1 (L1) cache, as well as a 2 KB prefetching buffer (L1P). All the cores on the same processor share a 32 MB level 2 (L2) cache and 16 GB of main memory. The compute nodes are connected via a 5D torus network with a total network bandwidth of 40 GB/s.

3 Results

We now present the results of our experiments on Vulcan, as well as a numerical analysis of the sources of the difficulty of the circuits described in [31, 5].

3.1 Simulation of a 49-qubit and a 56-qubit circuit on Vulcan

In the case of the 49-qubit circuit, the final quantum state is calculated in 2^{11} slices with 2^{38} amplitudes each. In the case of the 56-qubit circuit, only one slice with 2^{37} amplitudes is calculated (out of the 2^{19} such slices defining the final quantum state).

All experimental results are obtained over the course of two days. This time includes the time to set up the experiments described in this paper, as well as that to conduct additional experiments beyond the scope of what is described here.

Memory usage requires scaling to 4,096 nodes, with 64 TB of aggregate memory, for each (parallel) calculation. The theoretical minimum memory footprint to hold a slice of the state vector is less than 5 TB for the 49-qubit circuit (2^{38} complex doubles are used to store the 2^{38} amplitudes); it is common in the literature to report only the memory required for the state vector, e.g., [24]. In practice, experiments require more than 32 TB. The bulk of these operations require two large tensors to compute a result and CTF internal buffering introduces approximately a factor of 4 in overhead. Memory is also needed to reformat contraction operands for efficiency and for buffer space as messages are passed between nodes.

After computing the amplitudes, we analyze the distributions of the corresponding outcome probabilities to verify whether the observed distributions of probabilities adhere to the theoretically expected truncated exponential (Porter-Thomas) distributions [6]. Because outcome probabilities vary over several orders of magnitude and scale inversely with the number of outcomes, histograms are accumulated for log-transformed outcome probabilities $z = \log(Np)$, where $N = 2^n$, n being the number of qubits and p being an outcome probability. This mapping yields the expected truncated Gumbel distribution for the resulting histogram:

$$f_z(z) = \begin{cases} \frac{e^{z-e^z}}{1-e^{-N}} & z \leq n \ln 2 \\ 0 & \text{otherwise.} \end{cases} \quad (2)$$

Fig. 9 shows a plot of the histograms we obtain for an aggregation of the slices calculated for the 49-qubit circuit. Each histogram is an aggregation of 32 slices, and the 64 individual histograms are stacked together and rendered as a surface plot to better reveal variations between the histograms. As can be seen in this figure, the variations are concentrated at the extreme tail ends of the distribution where very low probabilities and, hence, very low bin counts are observed in the histograms. Such variations are expected in histograms whenever one is dealing with low bin counts. Fig. 9 reveals that the distributions of outcome probabilities across slices are virtually identical, demonstrating that this distribution is essentially isotropic across the quantum state, as expected, and there is an extremely close agreement between the observed and predicted distributions.

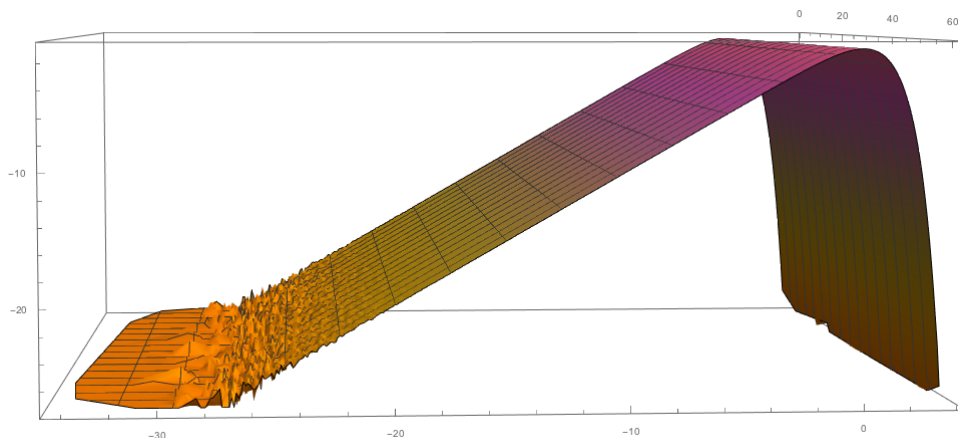


Figure 9: Histograms of log-transformed outcome probabilities for the individual slices of the 49-qubit circuit rendered together as a surface plot. The vertical axis is plotted on a log-scale.

Storage System	Size (PB)	Depth 55 Single Precision (hours)	Depth 55 Double Precision (hours)	Depth 83 Single Precision (hours)	Depth 83 Double Precision (hours)
Summit Burst Buffer	7	7.16	—	11.58	—
Summit File System	250	7.97	9.00	13.19	15.26
Sequoia File System	50	9.68	12.42	16.60	22.09
Vulcan File System	5	48.92	—	86.85	—

Table 1: Estimates of total run times, including secondary storage read/write times of various precisions, for the computation of full quantum state vectors of deep 7×7 -qubit circuits.

In the Supplementary Information, we discuss further quantum circuit simulations enabled by the ideas presented in this paper that involve circuits with more layers of gates. While we do not carry out these simulations, our framework allows us to verify that the memory and floating point operation requirements for these computations are viable on Vulcan or similar supercomputers. More specifically, combining targeted slicing with sporadic disk read/write operations, as already suggested by [24], we provide a method for simulating 7×7 universal random circuits up to arbitrary depth, writing all amplitudes to disk. Safe estimates summarized in Table 1 show that for a depth-83 circuit, this experiment could take ≈ 3.5 days on Vulcan, but would be completed in less than a day on Sequoia, the larger Blue Gene/Q supercomputer at Lawrence Livermore National Laboratory, or on Summit, the IBM-Power9/NVIDIA-Volta supercomputer recently installed at the Oak Ridge National Laboratory. Table 2 further summarizes the estimated percentage of time spent performing secondary storage access. Remarkably, we estimate that less than half the time would be spent performing disk I/O on the older Sequoia and Vulcan supercomputers, and that these estimates drop to around half of that for the newer Summit file system and to less than four percent using the Summit solid-state burst buffer. Importantly, we also describe in the Supplementary Information how this simulation approach can be generalized to handle arbitrary circuits and not merely universal random circuits.

Storage System	Depth 55 Single Precision (%)	Depth 55 Double Precision (%)	Depth 83 Single Precision (%)	Depth 83 Double Precision (%)
Summit Burst Buffer	3.18	—	3.93	—
Summit File System	12.98	22.98	15.68	27.12
Sequoia File System	28.33	44.15	33.02	49.65
Vulcan File System	43.30	—	48.78	—

Table 2: Estimates of the percentage of time spent performing secondary storage read/write operations during the computation of full quantum state vectors of 7×7 -qubit circuits of different depths, according to the desired numerical precision.

3.2 Analysis of circuit simulation difficulty

The results reported in the previous section are based on circuits generated according to the rules described in [6]. Subsequently, [31, 5] introduced several changes to the benchmark circuits, making them harder to simulate using the tensor-network-based methodologies known up to that point in time. In this section we present a quantitative assessment of the impact of these changes. We remark that some of these changes may not affect the difficulty of simulation when using techniques that are not based on tensor networks, e.g., Clifford-based approaches [9].

Three structural differences exist between the revised circuit generation rules and the original rules:

- The addition of a final layer of Hadamard gates;
- A different ordering of the patterned layers of CZ gates, as illustrated in Fig. 10²; and
- A different rule to randomly insert $X^{1/2}$, $Y^{1/2}$, and T single-qubit gates, to disallow sequences of $CZ - T - CZ$ gates from occurring along qubit lines.

Under both the original and revised rules, every circuit begins with a layer of Hadamard gates followed by layers of CZ gates, patterned as shown in Fig. 10 according to the original or revised rules. Under the original rules, single-qubit gates are inserted as follows:

- Wherever possible, insert a single-qubit gate on a qubit line immediately after a CZ gate subject to the following constraints:
 - If the most recent single-qubit gate applied to that qubit is a Hadamard gate, then insert a T gate;
 - Otherwise, randomly select the gate to insert from the set $\{X^{1/2}, Y^{1/2}, T\}$ subject to the constraint that the selected gate must be different from the most recent single-qubit gate applied to that qubit.

Under the revised rules, single-qubit gates are inserted as follows [43]:

- Wherever possible insert a single-qubit gate randomly selected from the set $\{X^{1/2}, Y^{1/2}\}$ on a qubit line immediately after a CZ gate.
- After performing the above insertions, wherever possible insert a T gate on a qubit line immediately after a $X^{1/2}$, $Y^{1/2}$, or H gate.

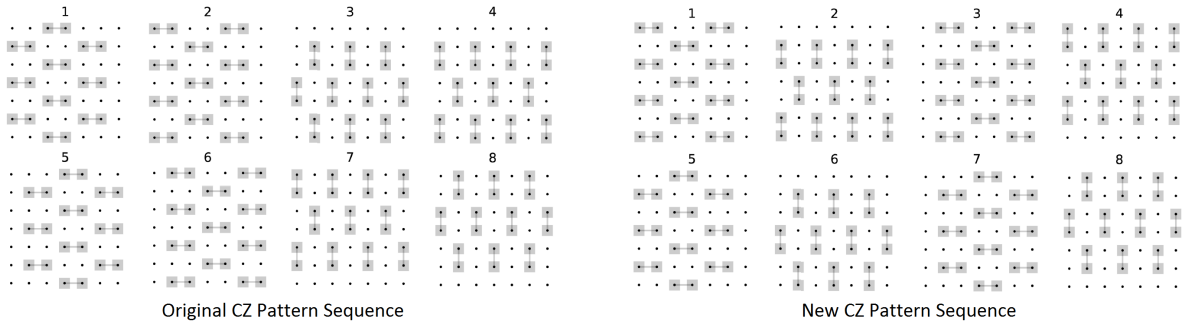


Figure 10: (a) *Left*. The sequence of patterned layers of CZ -gate defined by the rules described in [6]. (b) *Right*. The corresponding pattern sequence used in the circuits that are available in the GRSC public repository [5].

Viewing each structural change as an independent experimental treatment, we employ a full-factorial experimental design to evaluate the effects of all $2^3 = 8$ combinations of these treatments and the control (i.e., the original benchmark definition). Our quantitative assessment consists in estimating the Pareto frontiers of the computation vs. memory trade-off for each experimental combination, using the A^* optimization algorithm discussed earlier.

We report analysis results for both 49- and 56-qubit circuits. In the 49-qubit case, adding final layers of Hadamard gates to our original depth-27 circuit, and subtracting them from the corresponding `inst_7x7_28_0.txt` circuit in the GRSC public repository [5], provides us with four out of these eight combinations. To generate the other four we modify our circuit generation code, which we validate against circuits in the GRSC repository. In the 56-qubit case, the depth-23 circuit discussed in the previous section employs a 8×7 grid of qubits, whereas the GRSC repository contains circuits only for 7×8 grids. To resolve this mismatch, we use the `inst_7x8_24_0.txt` circuit from the GRSC repository both with and without the final layer of Hadamard gates, and we then generate the remaining six treatment combinations using our modified circuit generation code.

Somewhat surprisingly, the 7×8 , depth 23 circuit generated according to the original rules as described above is harder to simulate than the 8×7 , depth 23 circuit discussed in the previous section, as can be seen in the Pareto frontiers shown in Fig. 11. Indeed, when sufficient memory is available the 7×8 and 8×7 circuits require roughly the same levels of computation in terms of FLOPs per gate per amplitude; however, as available memory is reduced, the computational requirements of the 7×8 circuit begin to rise sharply as the memory threshold decreases, whereas the computational requirements of the 8×7 circuit continue to remain relatively flat. The computational requirements for the 8×7 circuit eventually rise sharply as well, but at a much smaller memory threshold. In the subsequent analysis, we use the location of such bends in the Pareto frontier to quantitatively compare the simulation difficulty of different circuits.

The Pareto frontiers obtained for the full-factorial experimental analysis of the 7×7 and 7×8 circuits are shown in Figs. 12 and 13, respectively. We use the following abbreviations:

- “Control” refers to the original circuit generation rules presented in [6];
- “H” refers to the experimental treatment of appending a final layer of Hadamard gates;
- “CZ” refers to the experimental treatment of replacing the original sequence of CZ layers presented in [6] with the revised sequence used in [5] as illustrated in Fig. 10; and

²There seems to be a small discrepancy between the pattern of the CZ gates reported in [43], and the circuits that are available in [5]. We use the pattern from [5].

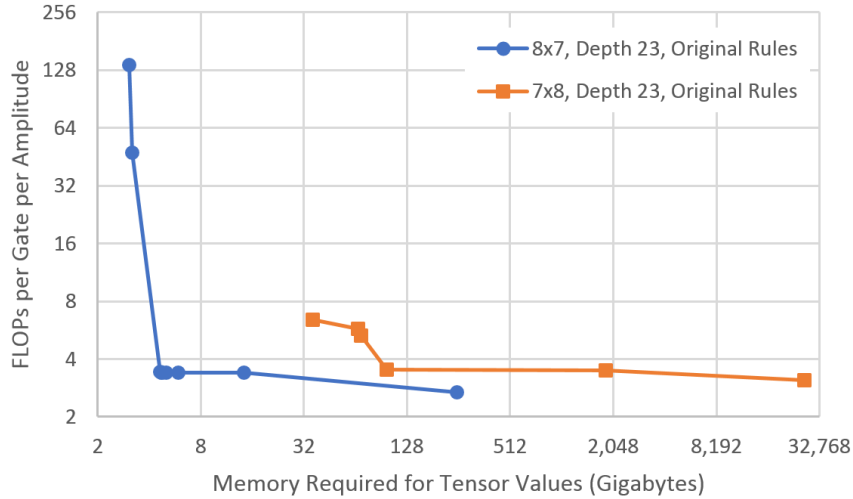


Figure 11: Pareto frontiers for 8×7 - and 7×8 -qubit, depth-23 circuits generated according to the rules described in [6].

- “SG” refers to the experimental treatment of replacing the original rules for inserting single-qubit gates presented in [6] with the revised rules used in [5] as described above.

We summarize the effect of the various changes in the following chain of inequalities indicating the relative difficulty (based on the location of the bend in the respective Pareto frontiers):

$$\text{Control} \approx \text{CZ} < \text{SG} \approx \text{SG \& H} < \text{H} < \text{CZ \& SG} < \text{CZ \& H} \approx \text{CZ \& SG \& H}.$$

To conclude, all changes in the circuit generation rules tend to increase the difficulty of simulation both individually and in combination, but in some cases the increase is modest (e.g., the revised sequence of CZ gates), while in other cases the increase is significant (e.g., the final layer of Hadamard gates, which appears to be the single most impactful change). Curiously, combining the new single-gate rules with a final layer of Hadamard gates yields circuits that are easier compared to inserting the Hadamards alone. Nevertheless, the combination of all changes dramatically increases the necessary computational resources, at least when using the tensor network techniques discussed in this paper. Note that all circuits considered still lie within reach of existing supercomputers.

4 Discussion

This paper presents a quantum circuit simulation methodology that introduces and extends several techniques. These techniques allowed us to simulate universal random circuits of a size that, for some time, were the largest to be simulated.

Among the techniques used in this paper and its arXiv preprint, a key contribution is the concept of contraction deferral. We provide a perspective on the recent literature in this area, highlighting the importance of contraction deferral, especially in combination with tensor slicing, see [15, 29, 13, 31, 43, 44, 45]. This combination has enabled the simulation of circuits much deeper than what is presented here. Another key contribution of our paper is the demonstration that the circuit partitioning and slicing techniques described in [24] can be extended to minimize data transfer at all levels of a system memory hierarchy. With this extension, secondary storage becomes a viable option for quantum circuit simulation. These techniques are not restricted to supercomputers, but could be leveraged on conventional

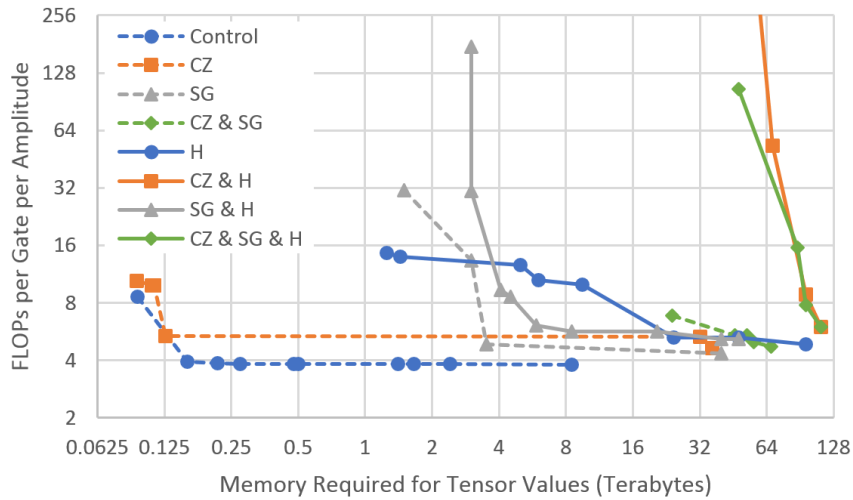


Figure 12: Pareto frontiers for the 7×7 -qubit, depth-27 circuits analyzed to assess the effects of the various changes in circuit generation rules introduced in [31, 5].

servers in order to expand the range of circuits that can be routinely simulated on those systems. An interesting question left to future exploration is whether combining sliced and non-sliced contraction deferral both along and across qubit lines can provide additional benefits, and to what extent.

Data availability

The datasets generated during and/or analysed during the current study are available from the corresponding author on reasonable request.

Competing interests

The authors declare that there are no competing interests.

Author contributions

The first three authors contributed equally to the overall conception, design, and drafting of the work, with E.P. contributing the idea of contraction deferral, J.A.G. contributing refinements to the tensor slicing methods, and G.N. contributing the directed hypergraph formulation and integer programming approach. The first four authors contributed equally to the conception of the approach to leveraging secondary storage. T.M. contributed refinements to the A^* algorithm. E.S. contributed improvements to the Cyclops Tensor Framework. E.W.D., E.T.H., and R.W. contributed to the planning of the experimental setup and its deployment on Vulcan, as well as to the analysis and interpretation of experimental results.

Acknowledgments

We are very grateful to Jonathan L. DuBois, Jay Gambetta, Ramis Movassagh, John A. Smolin, Frederick H. Streitz, Maika Takita, Robert Walkup, and Christopher J. Wood. Work of Thomas Magerlein was performed during an internship at the IBM T.J. Watson Research Center. Work of Erik W. Draeger and Eric T. Holland was performed under the auspices of the U.S. Department of Energy by the Lawrence

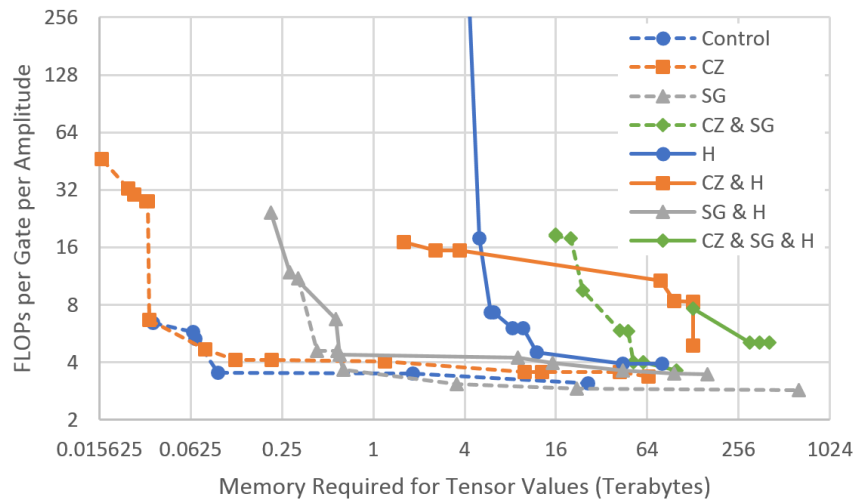


Figure 13: Pareto frontiers for the 7×8 -qubit, depth-23 circuits analyzed to assess the effects of the various changes in circuit generation rules introduced in [31, 5].

Livermore National Laboratory under Contract No. DE-AC52-07NA27344. This work was supported in part by the Laboratory Directed Research and Development under Grant No. 16-SI-004.

A Supplementary Information

The majority of this appendix is devoted to a detailed explanation of the mathematical foundations of our quantum circuit simulation methodology. Some of the concepts are repeated from the main text, but here we provide a more formal exposition that is useful to give a precise description of the algorithms. Based on these foundations, we describe a methodology capable of simulating deep 49-qubit circuits, up to arbitrary depth, giving a safe estimate of the required wall-clock time to show feasibility of such simulations. We also present an integer programming model that describes the space of feasible circuit partitionings considered by our methodology. The model can be used to search for partitionings with the desired properties. Finally, we discuss the relationship between our hypergraph representation with that of [32, 7].

A.1 Preliminaries

The description of diagonal tensors in the main text of the paper emphasizes that input index labels can carry over to output index labels, which may lead to the same index label appearing multiple times when there is a connected sequence of diagonal gates. For separable gates, one can use the corresponding diagonal gate in the tensor representation — adjusting the output indices to account for the permutation whenever the tensor is contracted, see below. We therefore define a *tensor network* as a hypergraph $G = (V, E, \lambda)$ consisting of:

- A vertex set V , such that each tensor is associated with a vertex.
- A hyperedge multiset E , such that each hyperedge e is an ordered subset of 2^V .
- A labeling function λ that associates a unique index label with each hyperedge $e \in E$.

For every hyperedge $e \in E$, we call *tail* the first node of e , *head* the last node of e .

The literature contains some examples of this type of tensor networks, see e.g., [10, 40], but to the best of our knowledge these concepts were not formalized and systematically used in the context of quantum circuit simulation.

Contractions can be defined on the type of tensor network indicated above. Since, as is discussed in the main text, our simulation algorithm also employs contractions between non-adjacent nodes, which are not standard in the tensor network literature, we give our own definition of contraction. Given a tensor network $G = (V, E, \lambda)$ and two vertices $u, v \in V$, we define a *contraction* of u, v as the tensor network $G' = (V', E', \lambda')$ such that:

- $V' = V \setminus \{u, v\} \cup \{w\}$, where w is a new node.
- E' is obtained from E by replacing, for each hyperedge, each maximal occurrence of a subsequence containing only u and v with w . The label $\lambda(e')$ for a contracted hyperedge e' is the same as the label $\lambda(e)$ for the original hyperedge e .
- The tensor T associated with w is obtained as follows. Let A be the tensor associated with u , B the tensor associated with v . Let S_{uv} be the set of index labels associated with hyperedges of the form $\{u, v\}$, S_{vu} the set of index labels associated with hyperedges of the form $\{v, u\}$. We distinguish between output indices, associated with a dual space (e.g., the rows of a matrix), and input indices, associated with a primal space (e.g., the columns of a matrix). In terms of notation, when subscripting tensors we indicate output indices before the comma, and input indices after the comma. Let I_A (resp. I_B) be the set of all input index labels for A (resp. B), O_A (resp. O_B) be the set of all output index labels for A (resp. B). Thus, the tensors A, B can be written as:

$$A_{\{k\}_{k \in S_{uv}} \{\ell\}_{\ell \in O_A \setminus S_{uv}}, \{i\}_{i \in S_{vu}} \{j\}_{j \in I_A \setminus S_{vu}}}, \quad B_{\{i\}_{i \in S_{vu}} \{n\}_{n \in O_B \setminus S_{vu}}, \{k\}_{k \in S_{uv}} \{m\}_{m \in I_B \setminus S_{uv}}}.$$

The tensor T is then defined as:

$$T_{\{\ell\}_{\ell \in O_A \setminus S_{uv}} \{n\}_{n \in O_B \setminus S_{vu}} \{j\}_{j \in I_A \setminus S_{vu}} \{m\}_{m \in I_B \setminus S_{uv}}} := \sum_{\{i\}_{i \in S_{vu}}} \sum_{\{k\}_{k \in S_{uv}}} A_{\{k\}} \{ \ell \}_{\ell \in O_A \setminus S_{uv}} \{i\} \{j\}_{j \in I_A \setminus S_{vu}} B_{\{i\}} \{n\}_{n \in O_B \setminus S_{vu}} \{k\} \{m\}_{m \in I_B \setminus S_{uv}}. \quad (3)$$

We highlight some special cases of the above definition. “Traditional” tensor network contractions occur when the edges $\{u, v\}$ or $\{v, u\}$ exist. In case $S_{uv} = S_{vu} = \emptyset$, the tensor contraction is an outer product between A and B . If A and B are diagonal, T is diagonal.

It is straightforward to note that given any set of nodes, any sequence of pairwise contractions that contracts the entire set yields the same outcome, regardless of the order (although the computational cost of the contraction may depend on such order). Thus, the concept of contraction generalizes naturally to sets of vertices: given a tensor network $G = (V, E, \lambda)$ and a subset of nodes $C \subseteq V$, a contraction of C is a tensor network $G' = (V', E', \lambda')$ obtained by performing pairwise contractions of nodes in C , in any order, until C collapses to a single node.

A.2 Simulation of quantum circuits

A *quantum circuit* on q qubits with depth D is a tensor network with the following properties:

- There are q rank-1 nodes associated with the tensor $|0\rangle$, called the “initial state”.
- There are q hyperedges whose head is a rank-1 node associated with the tensor $\langle 0|$, or a rank-1 node associated with the tensor $\langle 1|$, or a special node “O” that is not associated with any tensor and cannot be contracted, representing “open wires.” The heads of these q hyperedges are called the “output state.”
- Every node in the graph that is not an initial or output state is such that its input rank is equal to the output rank.
- All hyperedges are directed away from the initial state and toward the output state, i.e., there is a topological ordering of the graph such that the initial state precedes every other node, and the output state follows every other node.
- The maximum number of nodes on any path from the initial state to the output state is $D + 2$.

It follows from this definition that the graph can be partitioned into $D + 2$ sets of nodes (“layers”) with the property that each layer has at most q input hyperedges and q output hyperedges (the “qubit lines”). While we assume that every non-boundary tensor in a quantum circuit is either a rank-2 tensor (single-qubit gate) or a rank-4 tensor (two-qubit gate), most of our analysis directly applies to quantum circuits with gates that involve more than two qubits.

Given a quantum circuit $G = (V, E, \lambda)$ on q qubits, a *simulation strategy* for G is a sequence of contractions on G that contracts every node except the special node “O.” The node “O” is special precisely because it does not represent a tensor and is therefore not contracted.

We now come to defining the computational requirements for contractions, in terms of memory occupation and number of operations. We are interested in giving upper bounds to such costs. For this, we have to start mixing purely theoretical considerations with practical considerations. We assume that we have access to both primary and secondary storage: primary storage is a fast but more scarcely available resource, e.g., RAM, while secondary storage is slower but available in larger capacities, e.g., disk.

Assume we are given a quantum circuit $G = (V, E, \lambda)$ and a set of nodes $C \subseteq V$ to contract that would result in a rank n tensor. Assume further that there are m hyperedges that are fully contained in C . The result of the contraction takes space $O(2^n)$, and this is a space requirement that cannot be avoided. However, if such a contraction is the final goal of the computation, then the result of the contraction can be stored to disk rather than kept in RAM. Given these considerations, the *computational cost* of a simulation strategy is given by the number of floating point operations to perform the simulation. Its *memory cost* is the amount of space in primary and secondary storage that is required to store all intermediate tensors, i.e., all tensors except the final tensor connected to the special node “O.”

A.3 Asymptotic performance of quantum circuit simulation strategies

For the sake of completeness, we discuss the asymptotic performance of the most well-known circuit simulation strategies; the discussion in this section considers primary storage only. There are two very well-known ways to perform simulation of a circuit with q qubits and depth D , having different computational cost.

The first approach, sometimes called the “Schrödinger approach,” consists of contracting the circuit in layers. Given the topological ordering of the circuit, we can partition the circuit into $D + 2$ sets V_0, \dots, V_{D+1} such that V_0 contains the initial state, V_{D+1} the output state, and there is no hyperedge fully contained in each V_d . We first contract V_0 , which creates a $O(2^q)$ -size tensor, and then iteratively contract the newly created node with V_d , one node at a time, for $d = 1, \dots, D + 1$. Since there are no interior hyperedges for any of the sets V_d , every contraction has memory and computational cost $O(2^q)$, for a total of $O(D2^q)$ flops and $O(2^q)$ memory.

The second approach, sometimes called the “Feynman approach,” consists of contracting the entire network in one step, producing the output amplitudes one at a time by contracting all interior hyperedges. This amounts to evaluating each amplitude by summing over all possible paths. Assume that there are n open output wires, i.e., hyperedges whose head is “O.” Since the number of hyperedges in the circuit is $O(qD)$, the total computational cost is then $O(2^{n+qD})$, whereas memory occupation is $O(nD)$.

Recent work in the area provides better upper bounds. The paper [32] shows that the simulation of quantum circuits can be performed in time exponential in the treewidth of the underlying tensor network representation. The setting of [32] assumes that there is a full set of q output states $\langle 0|$ or $\langle 1|$, i.e., we are interested in computing only one of the state amplitudes at the end of the circuit. In this setting, simulating a circuit amounts to contracting the entire tensor network to a single node, obtaining a scalar. To this end, the paper [32] proposes a simulation strategy that always contracts adjacent nodes, according to an order obtained via a tree decomposition of the line graph of the tensor network. This yields a simulation strategy with cost (both computational and memory) exponential in the treewidth of said graph, which is within a multiplicative factor of the treewidth of the tensor network. For a discussion of treewidth and tree decompositions in combinatorial optimization, see [3].

The paper [1] introduces a simulation strategy that yields the best known upper bounds to date. For a general circuit, by recursively splitting the circuit in half according to the layers (i.e., creating two circuits of depth $D/2$, then four circuits of depth $D/4$, and so on), [1] gives an algorithm that takes $O(q(2D)^{q+1})$ time and $O(q \log D)$ memory. Specializing the algorithm to quantum circuits with an underlying two-dimensional grid connectivity graph, the running time decreases to $O\left(2^n \left[1 + \left(\frac{D}{c\sqrt{q}}\right)^{q+1}\right]\right)$ and the space requirement increases to $O(Dq \log q)$. To accomplish this goal, [1] first recursively partitions each layer of the circuit, according to its grid structure, in smaller grids with few edges across the sets of the partition, called a cut set. Because of the grid structure, the number of edges in the cut set is $O(\sqrt{q})$. Then, each set of the partition is equivalent to a depth D circuit with a small number of qubits, and these subcircuits can be contracted independently, provided we allow for extra ranks in

the tensors to account for the cut-set, and for the computational cost of the final contraction of edges in the cut-set. Rather than performing a full contraction of the subcircuits in one step, [1] recursively splits the circuit in half according to the layers, as mentioned above. The combination of these two recursive splitting ideas (splitting qubits according to the grid structure, and splitting the layers in half) gives a simulation strategy with the specified runtime.

A.4 Slicing

Assume we are given a quantum circuit $G = (V, E, \lambda)$ and a set of nodes $C \subseteq V$ with m interior hyperedges and n hyperedges that contain at least one node in C and one node outside C . Choose $s < n$ hyperedges that leave C , and assume that we want to perform a contraction of C with some other set of tensors, C' . Trivially, we can contract C with computational cost $O(2^{n+m})$ and total memory cost $O(2^n + m)$, create a rank n tensor, and then perform the contraction with C' .

An alternative way to perform computation that takes advantage of parallel computing capabilities is usually referred to as *slicing*. The idea is as follows: for all the 2^s possible values of the chosen s hyperedges, contract C with the value for these hyperedges fixed, creating 2^s “sliced” tensors. Calculating each of the sliced tensors has computational cost $O(2^{n+m-s})$ and memory (primary storage) cost $O(2^{n-s} + m)$. We can then contract each of the sliced tensors with C' . We remark that there are 2^s sliced tensors, and if we multiply the costs to compute the sliced tensors by 2^s we obtain essentially the initial cost for the contraction of C . However, there are two potential advantages to be gained through slicing: the more obvious one is that the 2^s computations can be performed in parallel; the less obvious, but equally important, is that we may be able to reorder the tensor computation in such a way that no more than a few slices of size $O(2^{n-s} + m)$ have to be in primary storage at the same time — the smaller the slices, the higher in the memory stack they can reside. Our simulation scheme makes this explicit by periodically storing or reading slices to/from (primary or secondary) storage. An appropriate slicing strategy can lead to significant memory savings by essentially splitting large tensors into smaller parts that can be processed separately.

A.5 Our simulation strategy

Given the framework defined above, the simulation strategy that we propose consists of partitioning the tensor network associated with the circuit into a small number of tensors with manageable rank and few hyperedges between tensors. Within each of these tensors, corresponding to subcircuits, we perform contraction in layers in a manner similar to that of the Schrödinger strategy. Below we provide a more formal description. We assume here for simplicity that all output wires of the tensor network are open, i.e., connected to “O,” to output the full quantum state; if this is not the case, the upper bounds on memory costs given in this section can potentially be tightened depending on the structure of the quantum circuit. In terms of notation, given $W \subseteq V$, we define

$$\mathcal{C}[W] := \{e \in E : \exists u, v \in e \text{ such that } u \in W, v \notin W\},$$

i.e., the set of hyperedges crossing the boundary of W . With a slight abuse of notation, given $F \subseteq E$ and $W \subseteq V$, we denote by $W \setminus F := W \setminus \bigcup_{e \in F} e$; in other words, subtracting a set of edges F from a set of nodes W implies deleting from W the nodes appearing in F .

Partition the vertex set V of G into V_1, \dots, V_k , which we call “subcircuits”. For $i = 1, \dots, k$, let $E_i := \mathcal{C}[V_i]$ be the set of hyperedges that contain at least one node in V_i , but are not fully contained in V_i . The computation is divided into $t \geq 1$ steps, with input/output operations from/to secondary storage between consecutive steps (although as we will discuss later, these operations may be skipped if all the intermediate tensors fit in primary storage). The sequence $\sigma_1, \dots, \sigma_k$ is a *computation order with t steps*

if it is nondecreasing, $\bigcup_{i=1,\dots,k} \sigma_i = \{1, \dots, t\}$, and for every hyperedge e , denoting by $\{V_j\}_{j \in \Sigma_e}$ the ordered sequence of sets V_1, \dots, V_k with nonempty intersection with e , then the sequence $\{\sigma_j\}_{j \in \Sigma_e}$ is also nondecreasing. The numbers $\sigma_1, \dots, \sigma_k$ are called the *computation steps* of sets V_1, \dots, V_k . Since V_1, \dots, V_k is a partition, we can unambiguously assign to each node in V the computation step from the subcircuit it belongs to. This simplifies our exposition. According to this definition, every hyperedge is directed from lower-index computation steps to higher-index computation steps. Clearly there exists a computation order for any partition V_1, \dots, V_k , because $t = 1, \sigma_1 = \dots = \sigma_k = 1$ is valid. The special node “O” is assigned the final computation step index $t + 1$. For every $i = 1, \dots, k, v \in V_i$, we define $V(v) := V_i$ and $\sigma(v) = \sigma_i$.

The computation proceeds following the computation order $\sigma_1, \dots, \sigma_k$. Subcircuits contracted at a given computation step can be used to initialize tensors in subsequent computation steps if they meet certain requirements. Formally, we assume that a set $P \subset \{(i, j) : \sigma_j = \sigma_i + 1, i, j = 1, \dots, k\}$ of precedence relations is given:

$$V_i \prec V_j \quad \forall (i, j) \in P.$$

The relation $V_i \prec V_j$ implies that subcircuit V_i can be used to initialize subcircuit V_j , therefore when V_j is processed the only open ranks in V_i must be those of the hyperedges that connect it to V_j . Let

$$\Delta := \{e \in E : \exists u, v \in e \text{ such that } \sigma(v) > \sigma(u) \text{ and } V(u) \neq V(v)\}.$$

In other words, Δ is the set of hyperedges linking subcircuits in different computation steps that do not follow the \prec relation. We give below in Algorithm 1 a pseudocode description of our simulation strategy. In the description, we call S the set of hyperedges sliced up until that point. All edges in Δ are sliced in the course of the algorithm.

Algorithm 1 Outline of the simulation strategy.

```

1:  $S \leftarrow \Delta \cap E_1$ .
2: for  $i = 1, \dots, k$  do
3:   for all combinations of values for the hyperedges in  $S$  do
4:     contract  $V_i$ , loading the initial state vector from secondary storage and following the
       Schrödinger method
5:     if  $\sigma_{i+1} > \sigma_i$  then
6:       contract all tensors in  $\{V_j : \sigma_j = \sigma_i\}$  and store the resulting tensor to secondary storage
7:     end if
8:   end for
9:    $S \leftarrow S \cup (\Delta \cap E_{i+1})$ 
10: end for

```

We now analyze the computational and storage requirements of the crucial steps of the algorithm.

Proposition: At step 4 of Algorithm 1, let

$$m_i := \left| \mathcal{C}[V_i \setminus \Delta] \setminus \bigcup_{j: \sigma_j < \sigma_i} E_j \right|,$$

and ℓ_i be the number of layers within V_i in the topological ordering of the circuit G . Then step 4 can be executed in $O(\ell_i 2^{m_i})$ time requiring $O(2^{m_i})$ primary storage.

Proof. Consider the first layer of V_i in the topological ordering of the graph. By definition, there are at most $|\mathcal{C}[V_i]|$ hyperedges crossing the boundary of such layer. Since edges in Δ are sliced (i.e., their value is fixed in every iteration of the for loop at line 3), the tensors appearing in Δ are one-dimensional

and can be contracted in linear time without adding open ranks. We are left with the tensors in $V_i \setminus \Delta$, which can be contracted to a tensor of rank $\mathcal{C}[V_i \setminus \Delta]$. However, by construction all edges in $\bigcup_{j:\sigma_j < \sigma_i} E_j$ (i.e., edges coming from earlier layers of the circuit – notice that sliced edges are removed only once) connect V_i to a tensor that has already been fully contracted, and can be considered as the “initial state” of the first layer of V_i . Thus, the first layer of V_i is a tensor of rank at most m_i , which takes at most $O(2^{m_i})$ primary storage and $O(2^{m_i})$ time to construct. We can then proceed following the topological ordering, contracting each layer with the subsequent layer. Each such step requires $O(2^{m_i})$ time, and yields a tensor of size $O(2^{m_i})$. Overall, this implies that V_i can be contracted in time $O(\ell_i 2^{m_i})$ requiring $O(2^{m_i})$ primary storage, as indicated. ■

Proposition. At step 6 of Algorithm 1, let $C_i := \{V_j : \sigma_j = \sigma_i\}$ be the set of tensors to be contracted, $\Gamma_i := \{e \in E : \exists u, v \in e \text{ such that } u \in V_j, v \in V_h, j \neq h, V_j, V_h \in C_i\} \setminus \Delta$ the set of hyperedges to be contracted, and let $N_i := \{e \in E : \exists u, v \in e \text{ such that } \sigma(u) = \sigma_i \text{ and } \sigma(v) = \sigma_i + 1\} \setminus \Delta$ be the hyperedges acting as input to the next computation step that are not sliced. Then step 6 can be executed in $O(2^{|N_i| + |\Gamma_i|})$ time requiring $O(\sum_{j \in C_i} 2^{m_j})$ primary storage and $O(2^{|N_i|})$ secondary storage.

Proof. Consider the hyperedges leaving C_i . Those hyperedges that do not intersect with subcircuits with computation step $\sigma_i + 1$ must be in Δ , hence their value is fixed by the for loop. Thus, at every iteration of the for loop, we must compute a tensor of rank $|N_i|$. To perform the contraction of the tensors corresponding to the subcircuits in $|C_i|$ we typically store the input tensors in primary storage, requiring $O(\sum_{j \in C_i} 2^{m_j})$ space, and perform $O(2^{|\Gamma_i|})$ operations per element of the output tensor. The output can be stored to secondary storage. This yields the memory and computation costs indicated. ■

The two propositions above specify the memory and computational cost of the two main resource-intensive steps of Alg. 1. Notice that the hyperedges in Γ_i correspond precisely to the indices whose contraction has been deferred (entanglement indices), as discussed in the main text of the paper. Although the above description leaves open the possibility of slicing such indices (sliced contraction deferral), this was not done in our experiments. In principle, it might be possible to perform the computation in different ways that may be more efficient, hence our analysis only states upper bounds. We remark that the stated upper bounds hold for each iteration of the for loop for sliced hyperedges, hence to obtain the total computational and secondary storage cost one should multiply by $2^{|S|}$; however, primary storage requirements do not scale exponentially with $|S|$, because at every iteration of the for loop we can keep in memory only the tensors corresponding to the current values for sliced edges. Furthermore, the for loop can be parallelized very efficiently, as long as we ensure that all the tensor slices involved in a computation are available on a given compute node.

Based on the preceding analysis, our goal is to look for a decomposition of G into subcircuits so that the computational and memory requirements are as small as possible. As mentioned in the main text of this paper, the search for such a decomposition can be carried out in a heuristic manner or with exact algorithms such as branch-and-bound; this is the topic of a subsequent section. Typically, the bottleneck for the simulation is given by primary storage requirements. Indeed, since each subcircuit is simulated essentially using the Schrödinger method (with some additional bookkeeping for ranks corresponding to hyperedges that connect to subcircuits with the same computation step), primary memory is the scarcest resource for our simulation strategy. Finally, from a practical point of view one should consider deviations from the proposed strategy that better fit the available hardware. For example, for the simulation of the 7×7 , depth-27 and 8×7 , depth-23 circuits discussed in the main text we do not need secondary storage at all: the tensors to be stored to disk all fit in primary storage (one slice at a time), therefore we speed up the computation by skipping the disk read/write cycle.

Gate	Multiplications	Additions	Memory [bytes]
X	2^{n+1}	2^n	2^{n+4}
Y	2^{n+1}	2^n	2^{n+4}
Z	2^n	0	2^{n+4}
H	2^{n+1}	2^n	2^{n+4}
CX	2^{n+2}	$3 \cdot 2^n$	2^{n+4}
CZ	2^n	0	2^{n+4}

Table 3: Memory requirements and number of floating point of operations for some quantum gates, when applied to a n -qubit quantum state (2^n -dimensional double precision complex vector).

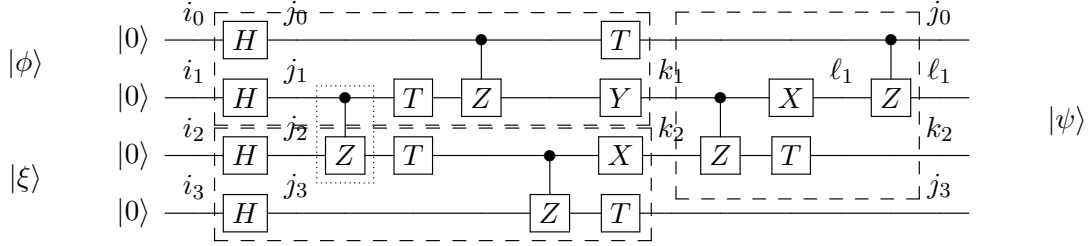


Figure 14: Example of a random 4×1 -qubit, depth 15 circuit generated according to [6]. The circuit can be contracted to 9 layers. The partitioning scheme is indicated in the figure. The tensor corresponding to the entangling gate in the second layer is assigned to the bottom subcircuit.

A.6 An example of possible computation schemes

We now provide a small example in order to illustrate the ideas discussed above. The memory and floating point requirements for the operations that will be used in this example are given in Table 3. Notice that these requirements assume that we want to compute the full state vector and each complex number requires 16 bytes of memory (two double-precision floating point numbers).

We consider a universal random circuit for a 4×1 grid of qubits with depth 15. It turns out that the generating rules produce many empty layers for this example and the circuit can be represented using 9 layers. Such a circuit is depicted in Fig. 14, together with a possible partitioning scheme. Using the notation described in the previous section, we have three subcircuits V_1, V_2, V_3 labeled $|\phi\rangle, |\xi\rangle, |\psi\rangle$ in Fig. 14. The computation order is $\sigma_1 = 1, \sigma_2 = 1, \sigma_3 = 2$; the precedence relations are $V_1 \prec V_3, V_2 \prec V_3$. The tensor for the first CZ gate in the circuit is assigned to V_2 , and there are three sliced hyperedges (indices j_0, k_2, j_3). To give a clearer description of how the proposed algorithm works, we give the full equations governing the state using the labeling indicated in the diagram (for simplicity, we use gate names to indicate the corresponding matrices):

$$\begin{aligned}
\phi_{j_0 k_1 j_1} &= T_{j_0, j_0} Y_{k_1, j_1} CZ_{j_0 j_1, j_0 j_1} T_{j_1, j_1} \sum_{i_0 \in \{0,1\}} H_{j_0, i_0} \delta_{i_0} \sum_{i_1 \in \{0,1\}} H_{j_1, i_1} \delta_{i_1} \\
\xi_{j_1 k_2 j_3} &= T_{j_3, j_3} \sum_{j_2 \in \{0,1\}} X_{k_2, j_2} CZ_{j_2 j_3, j_2 j_3} T_{j_2, j_2} CZ_{j_1 j_2, j_1 j_2} \sum_{i_2 \in \{0,1\}} H_{j_2, i_2} \delta_{i_2} \sum_{i_3 \in \{0,1\}} H_{j_3, i_3} \delta_{i_3} \\
\psi_{j_0 \ell_1 k_2 j_3} &= CZ_{j_0 \ell_1, j_0 \ell_1} T_{k_2, k_2} \sum_{k_1 \in \{0,1\}} X_{\ell_1, k_1} CZ_{k_1 k_2, k_1 k_2} \sum_{j_1 \in \{0,1\}} \phi_{j_0 k_1 j_1} \xi_{j_1 k_2 j_3}.
\end{aligned}$$

Note that, although the first CZ gate in the circuit is assigned to the bottom $|\xi\rangle$ subcircuit, we have to keep track of the extra j_1 index associated with that CZ gate in the top $|\phi\rangle$ subcircuit once the Y gate is introduced. In other words, j_1 becomes an entanglement index that cannot be contracted away until the tensors corresponding to the top $|\phi\rangle$ and bottom $|\xi\rangle$ subcircuits are combined: the precedence relations $V_1 \prec V_3, V_2 \prec V_3$ ensure that this is carried out before V_3 is computed. Because the hyperedges corresponding to indices j_0, k_2, j_3 are sliced, we never have to explicitly materialize the full state $|\psi\rangle$ in memory, and can work on slices. In this example, the final state can be computed in $2^3 = 8$ slices

using a state vector of size 2^1 for the computation of a slice, never allocating memory to hold a full 2^4 -dimensional state vector. Furthermore, we can decide to keep each slice in primary storage skipping all the secondary storage input/output operations indicated in Alg. 1, as the size of an individual slice does not exceed the available primary storage space.

The partitioning scheme for the 7×7 , depth-27 and 8×7 , depth-23 circuits is akin to the above example. With a similar graphic scheme (some details are omitted due to the circuit size), we depict in Fig. 15 the partitioning scheme used for the depth-27 and depth-23 simulations discussed in the main text of the paper. We remark that these circuits are constructed according to the rules of the first version of [6]. A revised benchmark was subsequently proposed [8], including circuits that are more difficult to simulate; at that time, our manuscript was already posted online and submitted for publication, therefore we did not run experiments on the revised benchmark.

A.7 Determining a computation scheme via integer programming

The problem of identifying a suitable computation scheme can be formulated as a discrete optimization problem. This is also the case for other simulation approaches discussed in the literature; most notably, papers based on tensor network contractions [32] require a treewidth decomposition of the circuit graph. In practice, such a decomposition is computed using heuristic or branch-and-bound algorithms; e.g., [7] reports running the branch-and-bound algorithm QuickBB “for a day” (quoted) to find a suitable decomposition. Here, we advocate an approach based on integer programming [34]. The main benefit of doing so is that there exist off-the-shelf software packages to solve discrete optimization problems articulated as integer programming problems. Thus, once the mathematical model for the problem is defined, a computation scheme can be determined automatically using such software. We now describe the integer programming model, and report a short summary of our computational experience.

Using notation from previous sections, we are given a hypergraph $G = (V, E)$ describing a circuit and our goal is to find (up to) k subcircuits V_1, \dots, V_k . For any positive integer n , we denote by $[n]$ the set $\{1, \dots, n\}$. The sequence $\sigma_1, \dots, \sigma_k$ of t computation steps is assumed to be given; this is without loss of generality because we can always pick k large and let some of the subcircuits be empty. We denote $T_c := \{j \in \{1, \dots, k\} : \sigma_j = c\}$, $c \in [t]$. For simplicity, we assume here that the set of precedence relations is fixed and equal to $P := \{(i, j) : \forall c \in [t-1], \forall i \in T_c, \forall j \in T_{c+1}\}$, which is what we use in all the examples and numerical tests discussed in this paper. It is not difficult to amend the integer programming model described below in a way such that the precedence relations are determined by an additional set of decision variables.

The decision variables of the integer programming model are:

- $x_{ij} \in \{0, 1\} \forall i \in [n], j \in [k]$. We write $x_{ij} = 1$ if $i \in V_j$, 0 if not.
- $s_e \in \{0, 1\} \forall e \in E$. We write $s_e = 1$ if edge $e \in E$ is sliced, 0 if not.
- $s_{ec} \in \{0, 1\} \forall e \in E, c \in [t-2]$. We write $s_{ec} = 1$ if edge $e \in E$ connects computation step c to computation step $c+2$ or greater, for $c \in [t-2]$, 0 if not. This is an auxiliary variable used to model s_e .
- $r_{ej} \in \{0, 1\} \forall e \in E, j \in [k]$. We write $r_{ej} = 1$ if edge $e \in E$ connects subcircuit j to a different subcircuit and must be included in rank computation, 0 otherwise.
- $m_j \in \mathbb{Z} \forall j \in [k]$. The variable m_j indicates the rank of subcircuit V_j .
- $z_c \in \mathbb{Z} \forall c \in [t]$. The variable z_c denotes the (ceiling of the) log of the complexity of computation step c (see step 6 of Algorithm 1).

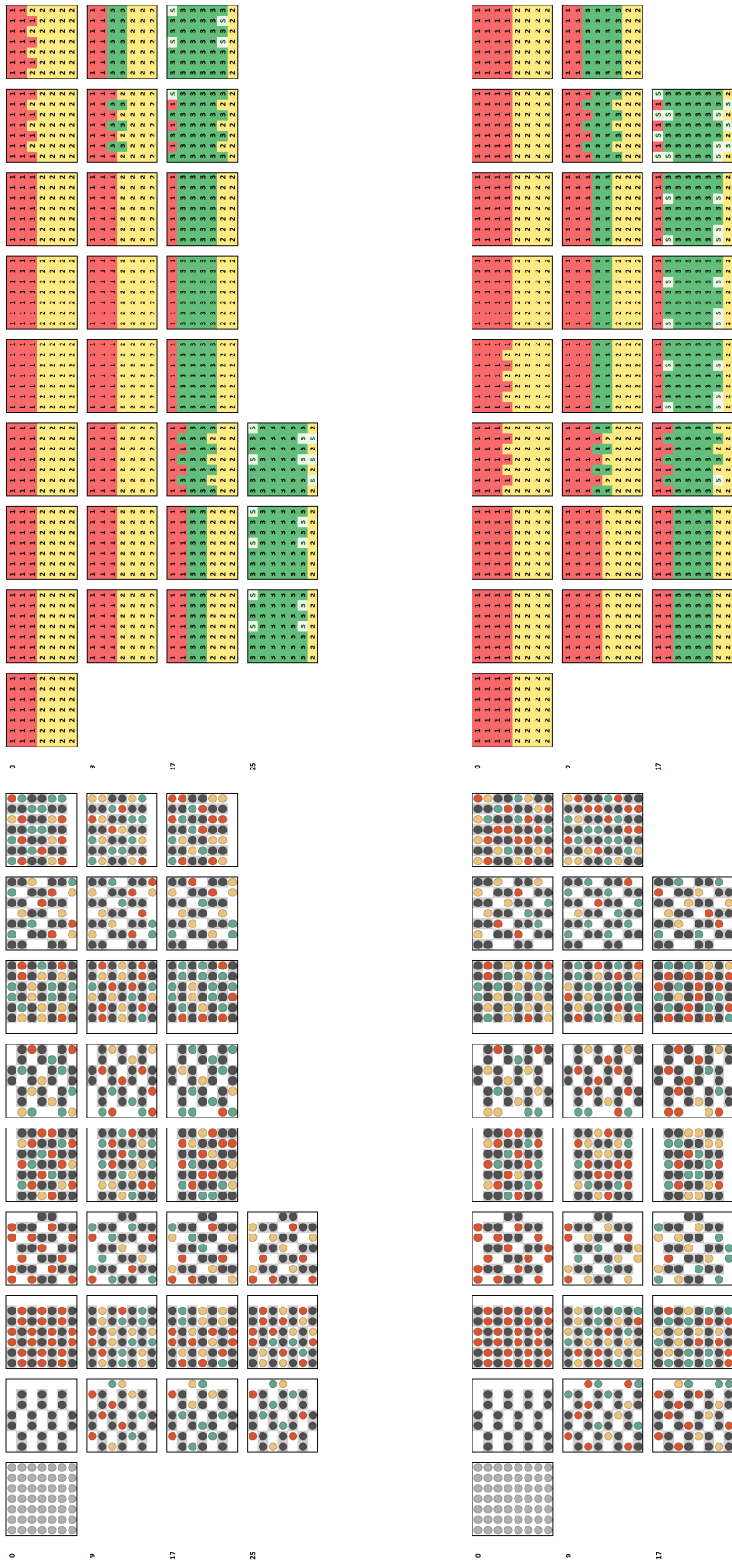


Figure 15: The 49-qubit, depth 27 circuit and the 56-qubit, depth 23 circuit are represented on the left. The figure on the right contains the respective partitioning. Qubits marked with an “S” can be sliced, as can the qubits in subcircuits 1 and 2 that are not involved in subcircuit 3 (i.e., those for which subcircuit 3 does not contain any gates applied to them).

To describe the space of possible circuit partitionings, we use the following set of constraints:

- $\forall i \in [n] : \sum_{j=1}^k x_{ij} = 1$. Each tensor (node in the graph) belongs to exactly one subcircuit.
- $\forall e \in E, \forall c \in [t-2] : 2s_{ec} \leq \sum_{j \in T_c} x_{\text{tail}(e)j} + \sum_{j \in \cup_{h \in [c+2, \dots, t]} T_h} x_{\text{head}(e)j}$. Variable s_{ec} can be 1 only if hyperedge e starts from tensor with computation step c and ends at a tensor with computation step $\geq c+2$.
- $\forall e \in E : s_e = \sum_{c \in [t-2]} s_{ec}$. Hyperedge e is sliced if and only if it connects computation step c and $c+2$, for some $c \in [t-2]$.
- $\forall e = \{v_1, \dots, v_\ell\} \in E, \forall p \in [\ell-1], \forall c \in [t-1] : \sum_{j \in T_{c+1}} x_{v_p j} + \sum_{j \in \cup_{h \in [c]} T_h} x_{v_{p+1} j} \leq 1$. The sequence of computation steps along any hyperedge must be nondecreasing.
- $\forall e = \{v_1, \dots, v_\ell\} \in E, \forall p \in [\ell], \forall q \in [\ell] \setminus \{p\}, \forall j \in [k], \forall h \in [k] \setminus \{j\} : x_{v_p j} + x_{v_q h} - s_e \leq r_{ej}$. If hyperedge e contains subcircuit j and h , and it is not sliced, it contributes to the rank of V_j . (These constraints are redundant when $q < p$ and $\sigma_h \geq \sigma_j$, so they can be dropped in that instance.)
- $\forall e = \{v_1, \dots, v_\ell\} \in E, \forall j \in [k] : x_{v_1 j} + s_e \leq r_{ej}$. If $\text{tail}(e) \in V_j$ and hyperedge e is sliced, then it contributes to the rank of V_j (as there is an edge crossing the partition that would not be counted otherwise).
- $\forall j \in [k] : m_j \geq \sum_{e \in E} r_{ej}$. Rank of subcircuit j .
- $\forall c \in [t] : z_c \geq \sum_{e \in E} \sum_{j \in T_c} r_{ej}$. Logarithm of the complexity of computation step c (see step 6 of Algorithm 1).

We remark that many of the constraints above are expressed as inequalities that only enforce lower bounds on the decision variables that model the rank of the subcircuits, i.e., tensors. As a consequence, there exist feasible solutions in which the decision variables indicate tensor ranks that are larger than the true value. This issue can be taken care of by minimizing all these variables via the objective function, or by imposing upper bounds. Notice that the model above allows many symmetric solutions (e.g., the indices of all subcircuits belonging to the same computation step are interchangeable). We break some symmetries by imposing a nonincreasing ordering in the size of the subcircuits at each computation step.

As the objective function of the problem our intent was to use $\min \max_{j \in [k]} m_j$, which can easily be modeled as a linear objective function with an additional variable, writing $\min w$ subject to $w \geq m_j \forall j \in [k]$. This corresponds to minimizing the rank of the largest subcircuit. To ensure that the decision variables modeling the tensor ranks are at their lower bound at the optimum, we add all these variables to the objective function, but with a smaller coefficient than the desired objective function $\min \max_{j \in [k]} m_j$. Thus, in our numerical experiments we use the objective function:

$$\min 100(\max_{j \in [k]} m_j) + \sum_{j \in [k]} m_j + \sum_{c \in [t]} z_c + \sum_{j \in [k]} (\max_{i \in V} x_{ij}), \quad (4)$$

where the purpose of the last term is to break ties between solutions in favor of solutions that use fewer subcircuits. One of the main advantage of using an integer programming model is its flexibility, therefore many alternative objective functions are possible; minimizing the maximum rank has the advantage that we do not have to explicitly model the exponential growth of memory requirements, which would be the case if we tried to minimize the total memory consumption $\sum_{j \in [k]} 2^{m_j}$.

We solve the integer programming model using IBM ILOG CPLEX 12.8 on a virtual machine instantiated in the cloud. The virtual machine has 32 Intel Xeon E5-2683 v4 @ 2.10GHz cores and 64 GB

Circuit	k	Upper bound	Lower bound
49 qubit, depth 27	4	38	27
49 qubit, depth 27	6	27	9
56 qubit, depth 23	4	38	29
56 qubit, depth 23	6	27	11

Table 4: Summary of the results of the automatic circuit partitioning based on integer programming. For each circuit and a given maximum number of subcircuits k , we report the best solution found and the best known lower bound after 5 hours.

RAM. In each run we impose a limit of 5 hours. The model is given to the solver as described above, without any further effort to generate additional valid inequalities that could improve performance, besides those that are automatically generated by CPLEX. We impose the additional constraint that at most 15 edges can be sliced, because otherwise we may obtain solutions that have too many such edges. This can be explained in light of the fact that sliced edges can reduce the rank of subcircuits, and the objective function used in these experiments considers tensor rank only, without taking the computation time into account. Results are summarized in Table 4. Notice that we report lower and upper bounds in terms of the (easier to understand) objective function $\min \max_{j \in [k]} m_j$, i.e., the rank of the largest tensor, rather than the modified objective function of Eq. 4. While the gap between upper and lower bounds is rather large when 6 subcircuits are considered, it is significantly smaller with 4 subcircuits, and shows that the partitionings used in the simulations discussed in this paper are nearly optimal. More importantly, the results confirm that the integer programming model is a viable approach to automatically determine computation schemes for circuits of these or similar sizes.

A.8 Computation of single amplitudes

The discussion so far has focused on the computation of the entire state vector, which is a natural outcome considering that our methodology is based on applying the Schrödinger approach to subcircuits. Computing a single amplitude $\langle x | Q | y \rangle$ for given basis states x, y is, in general, a simpler task. We can exploit the machinery described above to compute single amplitudes for circuits that are otherwise intractable with existing methodologies. In broad terms, we borrow inspiration from the recursive circuit partitioning schemes proposed in [1], but we depart from a purely recursive approach by constructing tensors for the resulting subcircuits using the computation scheme previously discussed.

Following [1], we first partition circuits depth-wise. Suppose we are given a quantum circuit of depth d implementing a unitary matrix Q . Calling L the unitary representing the first $\approx d/2$ layers of the circuit, and R the unitary representing the remaining layers, we have $Q = RL$. Our goal is to compute $\langle x | Q | y \rangle = \langle x | RL | y \rangle$. This can be accomplished by computing $L | y \rangle$ and $R^\dagger | x \rangle$ separately, then combining $(R^\dagger | x \rangle)^\dagger$ and $L | y \rangle$ to obtain $\langle x | RL | y \rangle$. Intuitively, this corresponds to simulating the circuit in input-to-output order for approximately half the total depth, and in output-to-input order for the remaining layers. The resulting tensors can then be contracted to obtain the desired amplitude. This idea was also developed, independently, in [29], but we contract the resulting tensors with a more efficient order than in [29].

We are interested in working with circuits whose state vectors cannot be fully stored in primary memory, so, in general, tensors corresponding to $L | y \rangle$ and $R^\dagger | x \rangle$ cannot be constructed directly. Instead, we apply the second partitioning scheme proposed in [1], which is to split the circuit row-wise. Assuming an $r \times c$ grid of qubits, the subcircuits corresponding to L and R would each be further partitioned into the top $\approx r/2$ rows of gates and the bottom remaining rows of gates. Following the approach described earlier, entanglement gates that bridge these top and bottom partitions would be assigned to

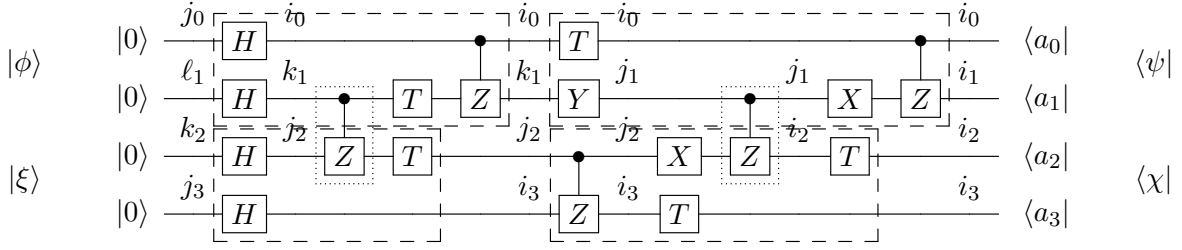


Figure 16: Example of a partitioning scheme to compute single amplitudes for the circuit in Fig. 14, simulating the circuit in input-to-output and output-to-input order. The tensors corresponding to the two dotted entangling gates are assigned to the top subcircuits.

one partition or the other, with entanglement indices introduced as appropriate. This assignment affects the memory requirements, therefore it is preferable to assign bridging gates to partitions so as to minimize the resulting memory occupation.

If ϕ and ξ are the top and bottom tensors constructed for the subcircuit corresponding to L , and if ψ and χ are the corresponding tensors for R , then contracting ϕ and ξ yields $L|y\rangle$ and contracting ψ and χ yields $R^\dagger|x\rangle$. Contracting all four tensors thus yields the desired amplitude $\langle x|RL|y\rangle$. Because we have complete freedom to choose the order of contraction, we can also consider contracting ϕ and ψ separately from ξ and χ , and then contracting the resulting tensors. This last order of contraction has desirable properties in terms of both memory requirements and floating-point operations.

Fig. 16 illustrates these ideas on the same circuit used for one of our previous examples. We give below the equations describing each of the subcircuits involved in the figure. In these equations, indices j_2 and i_2 correspond to the hyperedges of the CZ gates connecting the two wires in the middle that remain “open” in the corresponding tensor (i.e., not contracted within the tensor).

$$\begin{aligned}
\phi_{i_0 k_1 j_2} &= CZ_{i_0 k_1, i_0 k_1} T_{k_1, k_1} CZ_{k_1 j_2, k_1 j_2} \sum_{j_0 \in \{0,1\}} H_{i_0, j_0} \delta_{j_0} \sum_{\ell_1 \in \{0,1\}} H_{k_1, \ell_1} \delta_{\ell_1} \\
\xi_{j_2 i_3} &= T_{j_2, j_2} \sum_{k_2 \in \{0,1\}} H_{j_2, k_2} \delta_{k_2} \sum_{j_3 \in \{0,1\}} H_{i_3, j_3} \delta_{j_3} \\
\psi_{i_0 k_1 i_2} &= \left(\sum_{j_1 \in \{0,1\}} X_{i_1, j_1} CZ_{j_1 i_2, j_1 i_2} Y_{j_1, k_1} \right) T_{i_0, i_0} CZ_{i_0 i_1, i_0 i_1} \delta_{i_0 - a_0} \delta_{i_1 - a_1} \\
\chi_{j_2 i_3 i_2} &= CZ_{j_2 i_3, j_2 i_3} X_{i_2, j_2} T_{i_3, i_3} T_{i_2, i_2} \delta_{i_2 - a_2} \delta_{i_3 - a_3}
\end{aligned}$$

Given these four subcircuits, there are two natural ways to combine them to obtain the desired amplitude α : we can combine the tensors “vertically” first ($|\phi\rangle$ with $|\xi\rangle$, and $\langle\psi|$ with $\langle\chi|$) to obtain

$$\begin{aligned}
\lambda_{i_0 k_1 j_2 i_3} &= \sum_{j_2 \in \{0,1\}} \phi_{i_0 k_1 j_2} \xi_{j_2 i_3} \\
\rho_{i_0 k_1 j_2 i_3} &= \sum_{i_2 \in \{0,1\}} \psi_{i_0 k_1 i_2} \chi_{j_2 i_3 i_2} \\
\alpha &= \sum_{i_0, k_1, j_2, i_3 \in \{0,1\}} \lambda_{i_0 k_1 j_2 i_3} \rho_{i_0 k_1 j_2 i_3},
\end{aligned}$$

or “horizontally” first ($|\phi\rangle$ with $\langle\psi|$, and $|\xi\rangle$ with $\langle\chi|$) to obtain

$$\begin{aligned}
\sigma_{i_2 j_2} &= \sum_{i_0, k_1 \in \{0,1\}} \phi_{i_0 k_1 j_2} \psi_{i_0 k_1 i_2} \\
\omega_{i_2 j_2} &= \sum_{j_2, i_3 \in \{0,1\}} \xi_{j_2 i_3} \chi_{j_2 i_3 i_2} \\
\alpha &= \sum_{i_2, j_2 \in \{0,1\}} \sigma_{i_2 j_2} \omega_{i_2 j_2}.
\end{aligned}$$

It is easy to verify that the second approach is more efficient, creating intermediate tensors with smaller memory footprints and requiring fewer floating point operations.

We now describe a way to compute single amplitudes of universal random circuits with ~ 50 qubits and depth > 40 , which until very recently was thought to be out of reach for current technology. We discuss here the calculation of single amplitudes for a 7×7 -qubit, depth 46 universal random circuit. As

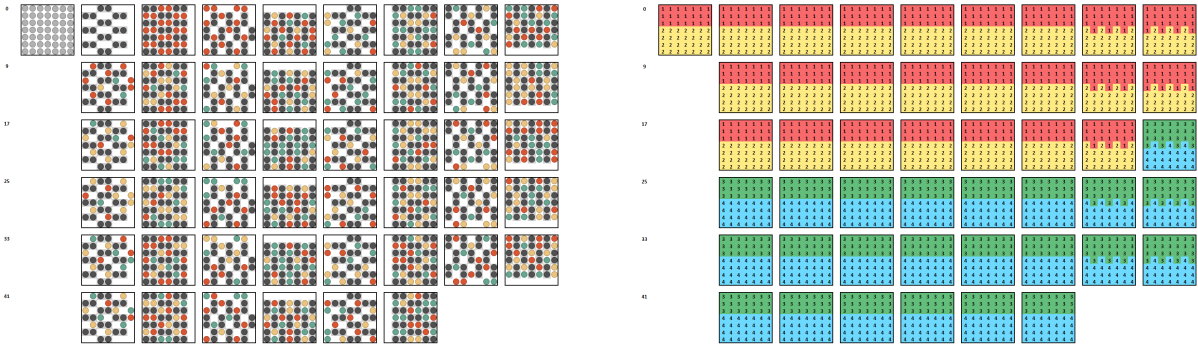


Figure 17: A 49-qubit, depth 46 circuit (left) and its partitioning (right).

discussed in the example above, we partition the circuit into four subcircuits: two depth-23 subcircuits simulated in an input-to-output fashion, which correspond to the first 23 layers and layer 0, and two depth-23 subcircuits simulated output-to-input, which correspond to the remaining 23 layers. Both pairs of subcircuits are partitioned at the boundary between the third and fourth rows of qubits, with the CZ gates that bridge this boundary assigned to the top subcircuit in each pair. This partitioning is illustrated in Fig. 17.

The four tensors constructed for these four subcircuits will incorporate various subsets of indices. One of these subsets of indices represents the quantum state of the qubits after applying the gates in layers 0 through 23. Let q_1, \dots, q_{49} be these indices with qubits numbered in left-to-right, top-to-bottom order. Fourteen additional entanglement indices also need to be introduced in the tensors representing layers 0 through 23 to account for the deferred contraction of the CZ gates that bridge the third and fourth rows in layers 7, 8, 15, and 16. Let e_1, \dots, e_{14} be these indices. Similarly, 14 additional entanglement indices need to be introduced in the tensors representing the remaining 23 layers to account for the deferred contraction of the CZ gates that bridge the third and fourth rows in layers 31, 32, 39, and 40. Let e_{15}, \dots, e_{28} be these indices. Because CZ gates are diagonal, additional entanglement indices are not needed for the bridging CZ gates at depths 23 and 24. Instead, q_{22}, \dots, q_{28} serve as these entanglement indices.

Following the nomenclature used in the above example, the four tensors calculated from the four subcircuits are then:

1. $\phi_{q_1 \dots q_{21} e_1 \dots e_{14} q_{23} q_{25} q_{27}}$ corresponding to the “top-left” subcircuit, requiring 4 TB of storage in double precision;
2. $\xi_{q_{22} \dots q_{49} e_1 \dots e_{14}}$ corresponding to the “bottom-left” subcircuit, requiring 64 TB of storage in double precision;
3. $\psi_{q_1 \dots q_{21} e_{15} \dots e_{28} q_{22} q_{24} q_{26} q_{28}}$ corresponding to the “top-right” subcircuit, requiring 8 TB of storage in double precision;
4. $\chi_{q_{22} \dots q_{49} e_{15} \dots e_{28}}$ corresponding to the “bottom-right” subcircuit, requiring 64 TB of storage in double precision;

Note that the total memory requirement of 140 TB for these four tensors lies well within the RAM limits of existing supercomputers. The horizontal-first contraction of the two top tensors and the two bottom tensors yields two intermediate tensors of 0.5 TB each, and the final amplitude calculation amounts to a

complex-valued dot product:

$$\begin{aligned}
\sigma_{q_{22}\dots q_{28}e_1\dots e_{28}} &= \sum_{q_1,\dots,q_{21}\in\{0,1\}} \phi_{q_1\dots q_{21}e_1\dots e_{14}q_{23}q_{25}q_{27}} \psi_{q_1\dots q_{21}e_{15}\dots e_{28}q_{22}q_{24}q_{26}q_{28}} \\
\omega_{q_{22}\dots q_{28}e_1\dots e_{28}} &= \sum_{q_{29},\dots,q_{49}\in\{0,1\}} \xi_{q_{22}\dots q_{49}e_1\dots e_{14}} \chi_{q_{22}\dots q_{49}e_{15}\dots e_{28}} \\
\alpha &= \sum_{q_{22},\dots,q_{28},e_1,\dots,e_{28}\in\{0,1\}} \sigma_{q_{22}\dots q_{28}e_1\dots e_{28}} \omega_{q_{22}\dots q_{28}e_1\dots e_{28}}.
\end{aligned}$$

Although we have not carried out the above simulations, expected execution times can nevertheless be estimated in a safe way (i.e., overestimated) by first developing parallelization schemes for the computations, then generating and testing benchmark codes that provide upper bounds on the computational loads per processing node for each subtask, and finally combining these execution times with estimated communication times based on the communication patterns and data transfer volumes dictated by the parallelization schemes. The estimated run times based on this methodology are 17.93 hours on the Vulcan supercomputer described earlier, and 4.76 hours on Sequoia, an IBM Blue Gene/Q supercomputer also located at Lawrence Livermore National Laboratory that is $4\times$ the size of Vulcan. To obtain safe upper bounds on the expected runtime, the benchmark codes responsible for 98.7% of the estimated times did not employ high-performance computing techniques such as cache blocking and loop unrolling. Faster run times should be achievable in actual, well-engineered implementations.

The recent paper [29] describes the computation of a single amplitude for a 7×7 , depth 55 circuit, using the idea of simulating the circuit in input-to-output order for approximately half the total depth, and in output-to-input order for the remaining layers. Once the two halves $L|y\rangle$ and $R^\dagger|x\rangle$ of the circuit are simulated, [29] computes the dot product $(R^\dagger|x\rangle)^\dagger L|y\rangle$ in slices in the most direct way, without changing the order of the tensor computation as discussed in this paper to reduce resource consumption. Such reordering does not appear to be necessary in the case of [29], likely because it uses a supercomputer (Sunway TaihuLight, ranked 1st in the TOP500 list of supercomputers as of November 2017) with significantly more memory than Vulcan or Sequoia.

A.9 Leveraging secondary storage

The paper [24] suggests that solid-state disk, or more generally secondary storage, could be used to supplement main memory in order to simulate circuits whose quantum states are too large to store in main memory alone. We combine the methods presented here with those in [24] to describe a viable computation scheme that exploits secondary storage to simulate deeper circuits than was thought possible.

The two methodologies are related by the fact that both involve circuit partitioning and both employ tensor slicing. In the case of [24], “global” qubits used to index across processing nodes correspond to tensor indices that are being sliced, and “local” qubits correspond to tensor indices that are being used to index into tensor slices stored on each processing node. In [24], circuits are partitioned so that all gates within a subcircuit can be applied to update quantum state tensors on a per-slice basis without communicating quantum state information between processing nodes. Zero-communication updates are possible when all non-diagonal gates in a subcircuit are being applied to “local” qubits only. Such updates are also possible for a handful of additional circumstances described in [24]. In effect, circuits are partitioned by selecting different subsets of “local” qubits and analyzing which gates can be applied to yield corresponding subcircuits. During simulation, communication between processing nodes occurs only when the simulation switches from one subcircuit to another. During these communication phases, the memory layouts of quantum state tensors are reorganized so that new subsets of indices are being used to “globally” index across processing nodes versus “locally” index within the memories of individual nodes, according to the needs of the next subcircuit to be simulated.

In the methods presented earlier, we considered circuit partitionings in which the resulting tensors either fit in available aggregate primary memory in their entirety, or slices of the resulting tensors could be computed using available primary memory based on other tensors already computed and stored in

primary memory. The resulting tensors and/or their slices will generally be larger than the primary memories of individual processing nodes, which represents a difference in the way tensor slicing is being viewed in this paper as compared to [24]. The techniques presented in [24] can be combined with those presented here to employ secondary storage when quantum states are too large to fit in aggregate primary memory. Because secondary storage is typically orders of magnitude slower than main memory, the viability of using it depends on the extent to which the number of read/write cycles can be minimized or overlapped with computation. To achieve such minimization, we first employ our decomposition ideas to partition the initial portions of a circuit so as to maximize the number of gates that can be simulated using available aggregate memory, with the resulting quantum state then calculated in slices and written to secondary storage. The partitioning methods discussed in [24] can then be applied to the remaining gates in the circuit with the number of “local” qubits set higher, according to the size of aggregate memory instead of the memory size available on individual processing nodes. The resulting tensor slices will then be much larger, allowing many more gates to be simulated before additional secondary-storage read/write cycles are needed. The resulting subcircuits can then be further partitioned into sub-subcircuits to minimize internode communication in the overall calculations.

We now provide a specific implementation of the above idea and estimate its computational cost. Simulating universal random circuits of ~ 50 qubits with arbitrary depth using secondary storage results in higher execution times due to the relatively high cost of disk read/write operations. However, we find both that the slowdown is considerably less than twofold for the instances under study, and that recent system advancements, such as NVRAM-based burst buffers, can have a highly beneficial effect on these run times. The larger memory pool available via secondary storage allows us to push the boundary of quantum circuit simulations even further. In order to do so, we observe that, by construction, universal random circuits have groups of qubits on the boundary of the grid that periodically do not interact with other qubits for several layers of gates. In particular, for circuits on a 7×7 grid, a group of 7 qubits at the boundary has two layers of two-qubit interactions with other rows or columns, followed by six layers without further interactions (only single-qubit gates or two-qubit gates within the group). For this reason, slicing these qubits is very effective: we can choose one of the boundary rows or columns, slice the corresponding qubits for six layers, and simulate the circuit applied to the remaining qubits independently. Recently, [24] used a similar observation to decide how to distribute computation across processors.

Our strategy consists in the following. We slice qubits at the boundary of the grid (e.g., the bottom row of the grid), simulating the remaining part of the circuit using the Schrödinger method with a tensor as large as our memory allows. The simulation is carried out for as many layers of gates as possible without introducing additional entanglement indices. Remarkably, for qubits on the opposite row/column (e.g., the top row of the grid) this allows us to apply over 30 layers of gates, whereas for qubits closer to the sliced qubits we can only progress for a handful of layers before we are forced to stop or increase memory occupancy. This produces several slices of the same size, which are stored to disk. To apply further gates we start a new subcircuit, slicing qubits in the row/column opposite to those sliced in the previous subcircuit (e.g., the top row of the grid), and simulating the rest of the circuit with the Schrödinger method. The initial state can be loaded from the slices stored on disk, and the process can be iterated. This yields a “wave” pattern in the subcircuits: each subcircuit starts from the top or bottom row of qubits, then extends to the rest of the circuit until it encompasses the row opposite to the starting set of qubits, at which point it shrinks back. We show the proposed circuit partitioning in Fig. 18. The specific example of Fig. 18 uses a circuit with depth 83, but the pattern used for subcircuits 4, 5 and 6 can be carried out indefinitely, adding further disk read/write operations. In the language of Alg. 1, there are 5 subcircuits: V_1, \dots, V_5 labeled 1, \dots , 5 in Fig. 18; we assign $\sigma_1 = \sigma_2 = 1, \sigma_3 = 2, \sigma_4 = 3, \sigma_5 = 4$, with precedence $V_1 \prec V_3, V_2 \prec V_3, V_3 \prec V_4, V_4 \prec V_5$. For every subcircuit $V_i, i \geq 3$, a row of qubits is sliced because the corresponding hyperedges connect V_{i-1} to V_{i+1} (if any non-diagonal single-qubit

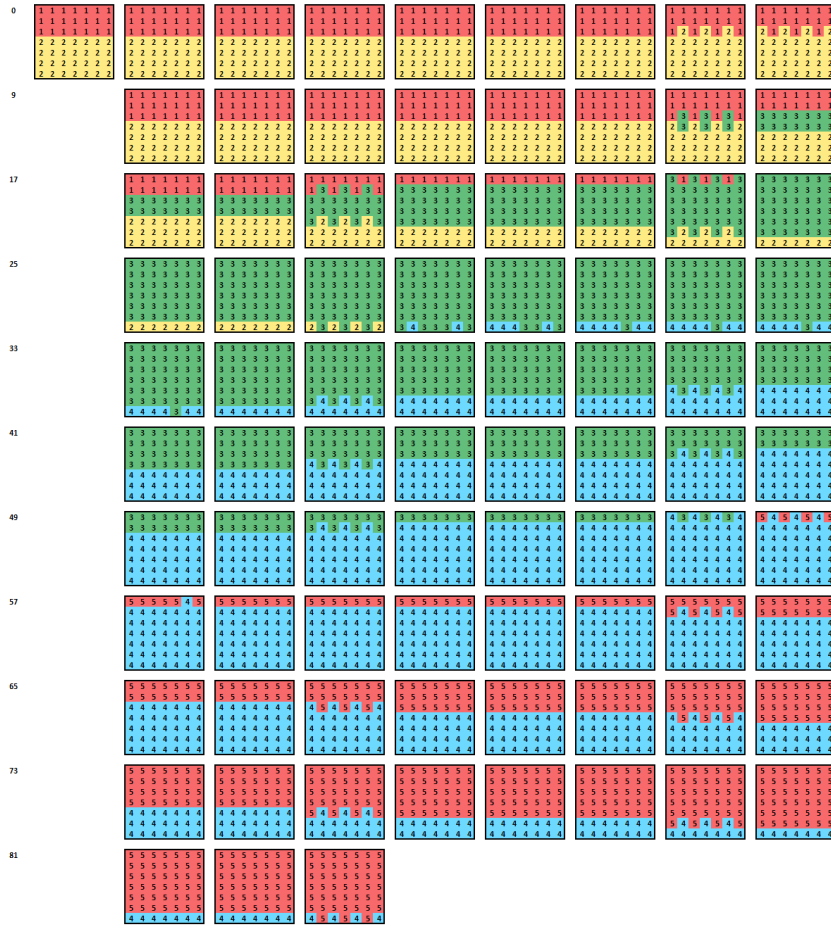


Figure 18: Partitioning of a 49-qubit, depth 83 circuit.

gates are applied on these qubits, instead of just one hyperedge per qubit we could have several shorter ones, which we would also slice).

For circuits of this size, it is important that the simulation algorithm is well-engineered in all of its aspects. Thus, we describe here the implementation choices that we used to estimate run times. We discuss a depth-83 circuit; the tables provide data for a depth-55 circuit as well.

Tensors for V_1 and V_2 in Fig. 18 are the first to be calculated, and the resulting pair of tensors is contracted one slice at a time. The slicing process proceeds by looping over the possible values for qubits 43–49 and slicing the tensor for V_2 on these values prior to performing the contraction with the tensor for V_1 . For each of the 128 resulting slices, the gates belonging to V_3 in Fig. 18 are applied to the contraction results and the resulting updated slices are transferred to secondary storage. This process of slicing, contracting, applying gates, and sending results to secondary storage is repeated 128 times, once for each of the 128 possible values of qubits 43–49. The gates belonging to V_4 in Fig. 18 are applied to the intermediate results that were transferred to secondary storage. These gate applications can also be performed in slices, this time slicing on qubits 1–7. To ensure the retrieval from secondary storage is performed efficiently, data can be organized in secondary storage as 2^{14} logical files indexed by the values of qubits 1–7 and 43–49, wherein each logical file contains 2^{35} complex amplitudes corresponding to qubits 8–42. Thus, in the phase discussed above of applying gates in V_3 , for each of the 128 values of qubits 43–49 that are being sliced, 128 logical files are written to secondary storage, corresponding to the 128 possible values of qubits 1–7. In the phase that applies the gates in V_4 ,

Subcircuit	Num Gates	Compute Time (hours)	All-to-All Time (hours)	Total (hours)
1	215	0.00	0.00	0.00
2	336	0.00	0.01	0.01
Contract	N/A	0.39	0.00	0.39
3	621	0.94	3.05	3.98
4	346	0.52	2.03	2.55
Total	1518	1.85	5.08	6.93

Table 5: Estimated computation and communication times for a 7×7 -qubit, depth 55 random circuit simulated on the equivalent of 4096 nodes of a Cori-II-class supercomputer. Time estimates do not include secondary storage access.

Subcircuit	Num Gates	Compute Time (hours)	All-to-All Time (hours)	Total (hours)
1	215	0.00	0.00	0.00
2	336	0.00	0.01	0.01
Contract	N/A	0.39	0.00	0.39
3	618	0.93	3.05	3.98
4	756	1.14	3.05	4.19
5	348	0.53	2.03	2.56
Total	2273	2.99	8.13	11.12

Table 6: Estimated computation and communication times for a 7×7 -qubit, depth 83 random circuit simulated on the equivalent of 4096 nodes of a Cori-II-class supercomputer. Time estimates do not include secondary storage access.

for each of the 128 values of qubits 1–7 that are being sliced, 128 logical files are read from secondary storage, corresponding to the 128 possible values of qubits 43–49. Once these 128 files of amplitudes are loaded into memory, the gates in V_4 can be applied and each updated slice can be written back to storage; alternatively, the final amplitudes can be processed in-memory on a per-slice basis.

For a depth-55 circuit, the simulation process ends with V_4 (in fact, we only need to apply the gates in V_4 at depth ≤ 55). To continue the simulation to depth 83, we repeat the process for V_5 , shown in Fig. 18, to simulate the remaining gates. We proceed in the same manner as for V_4 , except this time, for each of the 128 values of qubits 43–49 that are now being sliced, 128 logical files are loaded from secondary storage corresponding to the 128 possible values of qubits 1–7.

The timing results in [24] can be used to estimate computation and communication times for the above calculations, assuming that the parallelization methods discussed in [24] are being used and one is running on the equivalent of 4096 nodes of a Cori-II-class supercomputer. These times are reported in Tables 5 (for depth 55) and 6 (for depth 83).

The estimated compute times for V_1 and V_2 presented in Tables 5 and 6 are obtained by scaling the 6×5 -qubit simulation times reported in Table 1 in [24] according to the number of gates. The tensor values for V_1 and V_2 can be calculated in an embarrassingly parallel fashion without communication, where the local tensors in each node have rank 28. Thus, a single-node, 30-qubit simulation provides an upper bound to these compute times.

Estimated compute times for all other rows in Tables 5 and 6 are obtained by using the percent-

Storage System	Size (PB)	Transfer Rate (TB/sec)	Single Precision (hours)	Double Precision (hours)
Summit Burst Buffer	7	10.00	0.23	
Summit File System	250	2.20	1.03	2.07
Sequoia File System	50	0.83	2.74	5.48
Vulcan File System	5	0.11	21.18	

Table 7: Secondary storage sizes available on certain IBM supercomputers, the corresponding transfer rates, and the times needed to write 2^{49} quantum amplitudes to secondary storage and then read them back assuming full sustained transfer rates. Summit is the IBM-Power9/NVIDIA-Volta supercomputer at the Oak Ridge National Laboratory.

Storage System	Compute (hours)	All-to-All (hours)	Single Precision Read/Write (hours)	Double Precision Read/Write (hours)	Single Precision Total (hours)	Double Precision Total (hours)
Summit Burst Buffer	1.85	5.08	0.23	–	7.16	–
Summit File System	1.85	5.08	1.03	2.07	7.97	9.00
Sequoia File System	1.85	5.08	2.74	5.48	9.68	12.42
Vulcan File System	7.40	20.33	21.18	–	48.92	–

Table 8: Estimates of total run times, including secondary storage read/write times, for the computation of the full state vector of a 7×7 , depth-55 circuit.

communication column reported in Table 1 in [24] to first decompose the reported simulation time for a 7×6 -qubit circuit into a per-gate compute time and a per-all-to-all communication and synchronization time. This per-gate compute time is scaled by multiplying by the number of gates in each of the subcircuits under consideration, and then further multiplying by the number of slices (i.e., 128). The 7×6 timing results reported in [24] are used because subcircuits 3, 4, and 5 in Fig. 18 correspond to 7×6 -qubit subcircuits and the tensor slices involved in their simulation have rank 42. The sliced tensor contraction results for V_1 and V_2 also have rank 42. These tensor contractions require 128 complex multiplies and 127 complex additions per amplitude. An upper bound to the compute time is estimated by assuming an equivalent circuit-size of 256 gates to model the execution time.

All-to-all communication and synchronization times are estimated using the decomposed per-all-to-all time discussed above together with Figure 5 in [24] to determine the number of all-to-all communication cycles that are needed as a function of the depths of each subcircuit. Accordingly, for a depth 55 circuit, V_3 should require three all-to-alls per slice, while V_4 should require only two all-to-alls per slice. Similarly, for a depth 83 circuit, V_3 and V_4 should each require three all-to-alls per slice, while V_5 should require only two all-to-alls per slice. In addition, one all-to-all would be needed after computing the tensor for V_2 to redistribute it in preparation for the contraction of V_1 and V_2 . Each of these sources of all-to-all communication are reflected in Tables 5 and 6.

Tables 8-9 shows estimated overall run times, obtained by combining Tables 7, 5 and 6. We remark that these estimates assume the equivalent of 4096 of Cori II’s 9304 compute nodes. Because Sequoia and Summit are both ranked higher than Cori II in terms of their High Performance Linpack benchmarks, these execution times should be achievable on both Sequoia and Summit, and they can likely be improved upon. Vulcan is four times smaller than Sequoia, and so the computation and communication times estimated for Sequoia were multiplied by four to produce entries for Vulcan. The above estimates are thus very safe. The secondary storage transfer time estimates are less safe, being solely based on

Storage System	Compute (hours)	All-to-All (hours)	Single Precision Read/Write (hours)	Double Precision Read/Write (hours)	Single Precision Total (hours)	Double Precision Total (hours)
Summit Burst Buffer	2.99	8.13	0.46	–	11.58	–
Summit File System	2.99	8.13	2.07	4.14	13.19	15.26
Sequoia File System	2.99	8.13	5.48	10.97	16.60	22.09
Vulcan File System	11.97	32.52	42.37	–	86.85	–

Table 9: Estimates of total run times, including secondary storage read/write times, for the computation of the full state vector of a 7×7 , depth-83 circuit.

published data transfer rates.

It should be noted that the overall run time estimates in Tables 8-9 are all dominated by the computation and communication times, and not the secondary storage transfer times. Because these secondary storage transfer times are not dominant, we can conclude that secondary storage provides a viable basis for simulating quantum circuits to arbitrary depth when quantum states are too large to fit in main memory alone. This concludes our analysis of computing times for deep circuits.

The preceding analysis provides several insights that can be used to arrive at an automated process for partitioning circuits to leverage secondary storage. The first is that data organization on secondary storage should remain fixed during simulation, so that previously stored amplitudes can simply be overwritten with updated amplitudes without incurring additional overhead. A second insight is that, in order to make such overwriting as efficient as possible, secondary storage should be organized into tensor slices (i.e., the logical files discussed above) in such a way that the “global” qubits used to index into secondary storage are always a superset of the “global” qubits used to slice the computations. In the above example, qubits 1–7 and 43–49 were used to index into secondary storage while the computations alternated between slicing on qubits 43–49 and on qubits 1–7.

We now describe a greedy optimization approach that can be employed to identify such supersets of “global” qubits while at the same time trying to maximize the number of gates processed in each read/write cycle. The latter is essentially a proxy to minimizing the number of read/write cycles. The optimization proceeds in two stages.

The first stage consists of applying a suitable in-memory circuit partitioning method (e.g., the A^* or integer programming approaches presented in this paper) to depth-truncated versions of the circuit to be simulated, in order to determine the maximum depth at which the circuit can be simulated entirely in-memory. The qubits that are identified for slicing at this maximum depth are then used as the “global” qubits for the first phase of simulation prior to writing to secondary storage. In determining which qubits can be sliced, single-qubit diagonal gates are treated as non-diagonal for the purpose of identifying slicing opportunities. The rationale is that subsequent stages of analysis, described below, do not make use of these properties, so, in order to maintain consistency, we neglect to leverage these properties in the first stage as well. The properties of single-qubit diagonal gates can be exploited to optimize the computations entailed by the first stage of circuit partitioning, but we do not consider them in the choice of “global” qubits that will determine the organization of secondary storage. The final step of this first stage of optimization is to analyze the circuit partitionings obtained by the above approach to determine which of the remaining gates in the circuit can be applied without requiring any additional memory or contractions between subcircuits.

For example, suppose that the circuits shown in Fig. 15 actually extend much deeper and that a circuit partitioning method determined that the 7×7 and 8×7 circuits could only be simulated in-memory to depths 27 and 23, respectively, using the illustrated partitionings. In each case, according to

the discussion above, the qubits interior to subcircuit 3 would not be sliced in the manner illustrated in Fig. 15 because the slicing of these qubits relies on the presence of corresponding single-qubit diagonal gates in subcircuit 3 of each circuit. Instead, for the 7×7 circuit, only qubits 43–49 would be sliced, and for the 8×7 circuit, qubits 1–7 and 50–56 would be sliced. When these subcircuits are then extended by adding as many subsequent gates as possible, subcircuit 3 of the 7×7 circuit would be extended as deep as depth 55, as illustrated in Fig. 18. Similarly, subcircuit 3 of the 8×7 circuit would be extended as deep as depth 39 (not illustrated), but the resulting extension of subcircuit 3 would form a diamond-shaped pattern instead of the triangular patterns that can be seen in Fig. 18 for the 7×7 circuit. Note that in both cases, slicing qubits interior to subcircuit 3 to exploit single-qubit diagonal gates would have interfered with these subcircuit extensions.

The second stage of optimization selects “global” qubits for subsequent circuit partitions in a greedy fashion that attempts to maximally extend the depth of simulation at each phase. The analysis proceeds by first identifying, for each qubit, the depth of the deepest gate applied to that qubit given the circuit partitioning constructed thus far. The greedy heuristic is to slice on those qubits that correspond to the deepest of these gates, choosing a sufficient number of such “global” qubits to enable the per-slice computations for the resulting subcircuit to be performed in available aggregate main memory. Ties among possible choices are broken either randomly or by performing a greedy look-ahead search to evaluate which subset of candidate “global” qubits leads to the greatest circuit depth and/or number of gates in the resulting subcircuit.

The heuristic of choosing “global” qubits according to the deepest gates guarantees that the corresponding “local” qubits for the resulting subcircuit will incorporate qubits associated with the shallowest gates in the previous subcircuit. Empirically, these latter qubits tend to be associated with the deepest gates in the new subcircuit, which gives rise to the “wave” patterns observed in Fig. 18 as discussed above. For example, in Fig. 18 qubits 43–49 are sliced in the first phase and they end up with the shallowest gates at depths 26 and 27, while qubits 1–7 have the deepest gates at depths 54 and 55. Subsequently selecting and slicing on qubits 1–7 in the second phase results in qubits 43–49 now having the deepest gates while qubits 1–7 have the shallowest gates. The pattern then repeats.

The above process of choosing “global” qubits according to the deepest gates in successive partitioning phases is repeated until the circuit is completely segmented into subcircuits. The union of the “global” qubits of these subcircuits becomes the set of “global” qubits used to organize secondary storage. The “local” qubits for secondary storage will thus always be a subset of the “local” qubits at each phase of computation, which implies that each tensor slice during a phase of computation corresponds to a set of tensor slices on secondary storage. This correspondence further implies that during simulation, appropriate sets of tensor slices on secondary storage are loaded into aggregate main memory, operated upon, and their updated values are then written back to secondary storage without affecting any of the other tensor slices in secondary storage. The proposed approach minimizes secondary storage traffic during each computational phase and the total number of computational phases, thus minimizing total secondary storage access, through good choices of “global” qubits and circuit partitionings.

Note that it is conceivable that there exist circuit topologies for which the above process might yield a union of “global” qubits that incorporates all or too many qubits, thereby making slice sizes too small to enable efficient secondary storage transfer. In this case the selection process must be constrained. The simplest (greedy) approach would be to set a threshold on the maximum number of “global” qubits (or equivalently on the minimum number of “local” qubits) that can be used to organize secondary storage and to then choose “global” qubits for circuit partitioning in the same manner as before, but with the choice of deepest gates restricted to previously selected “global” qubits once this threshold is met.

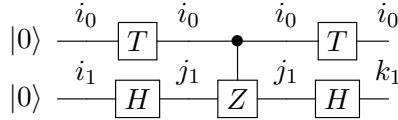


Figure 19: Example circuit for the line graph discussion.

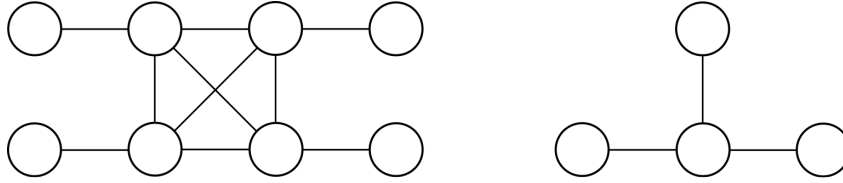


Figure 20: Line graph of the circuit in Fig. 19, using traditional tensor networks (left), and using the graphical model advocated in this paper (right).

A.10 On the graph representation of two-qubit gates

The tensor network representation used in our paper differs from [32] because of the presence of hyperedges. As discussed in the main text, this leads to a more accurate computation of the size of the tensors for diagonal gates, and allows more efficient circuit graph decompositions. As it turns out, our representation is equivalent to that of [7]. This is now explained in more detail.

We consider a two-qubit diagonal gate, since this is the only case in which differences between our paper and [32] arise. This difference is also the reason we sometimes choose to transform CX gates into CZ gates and Hadamards, to take advantage of the more efficient treatment of the diagonal CZ gates. The complexity of the simulation algorithm described in [32] depends on the treewidth of the line graph of the circuit graph. Given a hypergraph $G = (V, E)$, its line graph $G^* = (V^*, E^*)$ is defined by the vertex set $V^* := \{e \in E\}$ and the edge set $E^* := \{(e^1, e^2) \in V^* \times V^* : e^1 \cap e^2 \neq \emptyset\}$. Notice that this definition matches the traditional definition of line graphs when applied to a regular graph G (as opposed to a hypergraph). We show the difference between the line graph of our representation of the graph circuit, and that of [32], using the circuit given in Fig. 19. The hypergraph of the circuit in Fig. 19 has only four hyperedges because there are four different index labels in the circuit, while the traditional tensor network representation has eight — one for each wire segment. This leads to a 4-clique in the line graph of the traditional tensor network (Fig. 20, left), while the line graph of the hypergraph has only 2-cliques (Fig. 20, right). The reader can easily verify that the graphical model proposed in [7] in the context of a variable elimination algorithm yields exactly the same graph representation of the line graph of the hypergraph. This is due to the fact that both our hypergraph and the variable elimination model put more emphasis on the indices of the tensor network than in [32].

References

- [1] S. Aaronson and L. Chen. Complexity-theoretic foundations of quantum supremacy experiments. *arXiv preprint arXiv:1612.05903*, 2016.
- [2] R. J. Bartlett. Many-body perturbation theory and coupled cluster theory for electron correlation in molecules. *Annual Review of Physical Chemistry*, 32(1):359–401, 1981.
- [3] D. Bienstock and M. A. Langston. Algorithmic implications of the graph minor theorem. *Handbooks in Operations Research and Management Science*, 7:481–502, 1995.

- [4] L. S. Bishop, S. Bravyi, A. Cross, J. M. Gambetta, and J. Smolin. Quantum volume. Technical report, IBM T.J. Watson, 2017.
- [5] S. Boixo. Random quantum circuits for circuit sampling with superconducting qubits. *Available at <https://github.com/sboixo/GRCS>*, 2018.
- [6] S. Boixo, S. V. Isakov, V. N. Smelyanskiy, R. Babbush, N. Ding, Z. Jiang, M. J. Bremnen, J. M. Martinis, and H. Neven. Characterizing quantum supremacy in near-term devices. *Nature Physics*, 14(6):595–600, 2018.
- [7] S. Boixo, S. V. Isakov, V. N. Smelyanskiy, and H. Neven. Simulation of low-depth quantum circuits as complex undirected graphical models. *arXiv preprint arXiv:1712.05384*, 2017.
- [8] S. Boixo and C. Neill. The question of quantum supremacy, 2018.
- [9] S. Bravyi, D. Browne, P. Calpin, E. Campbell, D. Gosset, and M. Howard. Simulation of quantum circuits by low-rank stabilizer decompositions. *arXiv preprint arXiv:1808.00128*, 2018.
- [10] O. Buerschaper, M. Aguado, and G. Vidal. Explicit tensor network representation for the ground states of string-net models. *Physical Review B*, 79(8):085119, 2009.
- [11] D. Castelvecchi. Quantum cloud goes commercial. *Nature*, 543, 2017.
- [12] D. Castelvecchi. Quantum computers ready to leap out of the lab in 2017. *Nature*, 541:9–10, 2017.
- [13] J. Chen, F. Zhang, M. Chen, C. Huang, M. Newman, and Y. Shi. Classical simulation of intermediate-size quantum circuits. *arXiv preprint arXiv:1805.01450*, 2018.
- [14] M.-C. Chen, R. Li, L. Gan, X. Zhu, G. Yang, C.-Y. Lu, and J.-W. Pan. Quantum teleportation-inspired algorithm for sampling large random quantum circuits. *arXiv preprint arXiv:1901.05003*, 2019.
- [15] Z. Chen, Q. Zhou, C. Xue, X. Yang, G. Guo, and G. Guo. 64-qubit quantum circuit simulation. *arXiv preprint arXiv:1802.06952*, 2018.
- [16] L. Dagum and R. Menon. OpenMP: an industry standard API for shared-memory programming. *IEEE computational science and engineering*, 5(1):46–55, 1998.
- [17] E. Farhi and A. W. Harrow. Quantum supremacy through the quantum approximate optimization algorithm. *arXiv preprint arXiv:1602.07674*, 2016.
- [18] R. P. Feynman. Simulating physics with computers. *International journal of theoretical physics*, 21(6):467–488, 1982.
- [19] E. S. Fried, N. P. Sawaya, Y. Cao, I. D. Kivlichan, J. Romero, and A. Aspuru-Guzik. qTorch: The quantum tensor contraction handler. *arXiv preprint arXiv:1709.03636*, 2017.
- [20] J. M. Gambetta, J. M. Chow, and M. Steffen. Building logical qubits in a superconducting quantum computing system. *arXiv preprint arXiv:1510.04375*, 2015.
- [21] A. Gheorghiu, T. Kapourniotis, and E. Kashefi. Verification of quantum computation: An overview of existing approaches. *arXiv preprint arXiv:1709.06984*, 2017.
- [22] W. Gropp, E. Lusk, and A. Skjellum. *Using MPI: portable parallel programming with the message-passing interface*, volume 1. MIT press, 1999.

- [23] C. Guo, Y. Liu, M. Xiong, S. Xue, X. Fu, A. Huang, X. Qiang, P. Xu, J. Liu, S. Zheng, H.-L. Huang, M. Deng, D. Poletti, W.-S. Bao, and J. Wu. General-purpose quantum circuit simulator with projected entangled-pair states and the quantum supremacy frontier. *arXiv preprint arXiv:1905.08394*, 2019.
- [24] T. Häner and D. S. Steiger. 0.5 petabyte simulation of a 45-qubit quantum circuit. In *Proceedings of the International Conference for High Performance Computing, Networking, Storage and Analysis, SC '17*, pages 33:1–33:10, New York, NY, USA, 2017. ACM.
- [25] A. W. Harrow and A. Montanaro. Quantum computational supremacy. *Nature*, 549(7671):203, 2017.
- [26] E. Hart, N. Nilsson, and B. Raphael. A formal basis for the heuristic determination of minimum cost paths. *IEEE Transactions on Systems, Science and Cybernetics*, SSC-4(2):100–107, 1968.
- [27] A. W. Joshi. *Matrices and tensors in physics*. New Age International, 1995.
- [28] C. L. Lawson, R. J. Hanson, D. R. Kincaid, and F. T. Krogh. Basic linear algebra subprograms for Fortran usage. *ACM Transactions on Mathematical Software (TOMS)*, 5(3):308–323, 1979.
- [29] R. Li, B. Wu, M. Ying, X. Sun, and G. Yang. Quantum supremacy circuit simulation on sunway taihulight. *arXiv preprint arXiv:1804.04797*, 2018.
- [30] N. M. Linke, D. Maslov, M. Roetteler, S. Debnath, C. Figgatt, K. A. Landsman, K. Wright, and C. Monroe. Experimental comparison of two quantum computing architectures. *Proceedings of the National Academy of Sciences*, 114(13):3305–3310, 2017.
- [31] I. L. Markov, A. Fatima, S. V. Isakov, and S. Boixo. Quantum supremacy is both closer and farther than it appears. *arXiv preprint arXiv:1807.10749*, 2018.
- [32] I. L. Markov and Y. Shi. Simulating quantum computation by contracting tensor networks. *SIAM Journal on Computing*, 38(3):963–981, 2008.
- [33] H. McCraw, D. Terpstra, J. Dongarra, K. Davis, and M. R. Beyond the CPU: Hardware performance counter monitoring on Blue Gene/Q. In *Proceedings of the International Supercomputing Conference 2013*, volume 7905 of *LNCS*, pages 213–225, Heidelberg, June 2013. Springer.
- [34] G. L. Nemhauser and L. A. Wolsey. *Integer and Combinatorial Optimization*. Wiley, New York, 1988.
- [35] R. Orús. A practical introduction to tensor networks: Matrix product states and projected entangled pair states. *Annals of Physics*, 349:117–158, 2014.
- [36] E. Pednault. Quantum computing—breaking through the 49 qubit simulation barrier. *IBM Research Blog posting also posted on phys.org* (<https://www.ibm.com/blogs/research/2017/10/quantum-computing-barrier/> and <https://phys.org/news/2017-10-quantum-computingbreaking-qubit-simulation-barrier.html>), 2017.
- [37] E. Pednault, J. A. Gunnels, G. Nannicini, L. Horesh, T. Magerlein, E. Solomonik, and R. Wisnieff. Breaking the 49-qubit barrier in the simulation of quantum circuits. *arXiv preprint arXiv:1710.05867*, 2017.

- [38] J. Preskill. Quantum computing and the entanglement frontier. *arXiv preprint arXiv:1203.5813*, 2012.
- [39] M. Reed, L. DiCarlo, B. Johnson, L. Sun, D. Schuster, L. Frunzio, and R. Schoelkopf. High-fidelity readout in circuit quantum electrodynamics using the jaynes-cummings nonlinearity. *Physical review letters*, 105(17):173601, 2010.
- [40] M. B. Şahinoğlu, D. Williamson, N. Bultinck, M. Mariën, J. Haegeman, N. Schuch, and F. Verstraete. Characterizing topological order with matrix product operators. *arXiv preprint arXiv:1409.2150*, 2014.
- [41] E. Solomonik, D. Matthews, J. R. Hammond, J. F. Stanton, and J. Demmel. A massively parallel tensor contraction framework for coupled-cluster computations. *Journal of Parallel and Distributed Computing*, 74(12):3176–3190, 2014.
- [42] I. B. G. team. Design of the IBM Blue Gene/Q compute chip. *IBM Journal of Research and Development*, 57(1/2):1:1–1:13, Jan 2013.
- [43] B. Villalonga, S. Boixo, B. Nelson, C. Henze, E. Rieffel, R. Biswas, and S. Mandrà. A flexible high-performance simulator for the verification and benchmarking of quantum circuits implemented on real hardware. *arXiv preprint arXiv:1811.09599*, 2018.
- [44] B. Villalonga, D. Lyakh, S. Boixo, H. Neven, T. S. Humble, R. Biswas, E. G. Rieffel, A. Ho, and S. Mandrà. Establishing the quantum supremacy frontier with a 281 pflop/s simulation. *arXiv preprint arXiv:1905.00444*, 2019.
- [45] F. Zhang, C. Huang, M. Newman, J. Cai, H. Yu, Z. Tian, B. Yuan, H. Xu, J. Wu, X. Gao, J. Chen, M. Szegedy, and Y. Shi. Alibaba cloud quantum development kit: Large-scale classical simulation of quantum circuits. *arXiv preprint arXiv:1907.11217*, 2019.